Title: Recalibration of macrophage lipid metabolism underlies intracellular bacterial neuroinvasion

Authors: Zhou Sha[1, #], Kun Yang[2, #], Shoupeng Fu[3, #], Xiaoyong Tong[4, #], Hui Yang[1], Huiling Fang[1], Qianqian He[1], Ning Li[5, 6], Xinyu Shu[5, 6], Qi Liu[1], Yongliang Du[1], Beibei Fu[1], Yan Xiong[1], Dong Guo[1], Jing Liu[4], Qian Li[7], Hao Zeng[8], Rui Yao[9], Xushuo Zhang[10], Wenjin Guo[3], Xuhu Mao[7], Mian Long[5, 6, *], Xiaoyuan Lin[7, 11, *], Quanming Zou[8, *], Haibo Wu[1, *]

1 School of Life Sciences, Chongqing University, Chongqing 401331, China

2 Chongqing Public Health Medical Center, Chongqing 400036, China

3 School of Veterinary Medicine, Jilin University, Changchun 130062, China

4 School of Pharmaceutical Sciences, Chongqing University, Chongqing 401331, China

5 Center of Biomechanics and Bioengineering, Key Laboratory of Microgravity (National Microgravity Laboratory), and Beijing Key Laboratory of Engineered Construction and Mechanobiology, Institute of Mechanics, Chinese Academy of Sciences, Beijing 100190, China

6 School of Engineering Sciences, University of Chinese Academy of Sciences, Beijing 100049, China

7 Department of Clinical Microbiology and Immunology, College of Pharmacy and Laboratory Medicine, Army Medical University (Third Military Medical University),

Chongqing 400038, China.

8 National Engineering Research Center of Immunological, Department of Microbiology and Biochemical Pharmacy, College of Pharmacy and Laboratory Medicine, Army Medical University (Third Military Medical University), Chongqing 400038, China.

9 Department of Pathology, Chongqing Hygeia Hospital, Chongqing 401331, China

10 Zhejiang Toyouvax Biopharming, Hangzhou 311100, China

11 Institut für Virologie, Freie Universität Berlin, Robert-von-Ostertag-Str. 7-13, Berlin 14163, Germany.

# Equally Contributing Authors

* Corresponding authors

Mian Long, mlong@imech.ac.cn

Xiaoyuan Lin, linxiaoyuan23@163.com

Quanming Zou, qmzou2007@163.com

Haibo Wu, hbwu023@cqu.edu.cn

Abstract

Acute infection of the central nervous system is one of the most deadly diseases, but the mechanisms by which intracellular bacterial pathogens infiltrate the brain remain poorly understood. Phagocytic cells are usually recognized as the battlefield against intracellular bacteria; however, little is known about how the intracellular bacteria

take advantage of infected phagocytes to access the brain. Here, we identify that a novel $CD36^+$ foamy macrophage subpopulation is participated in the brain penetration of intracellular bacteria. Biomechanical analysis reveals that the abundant protrusions and adhesion molecules confer significant resistance to the mechanical stress of blood flow, thereby providing more opportunities for foamy macrophages to adhere on the vascular endothelial surface during the neuroinvasion. By applying metabolomics analysis, we show that macrophage lipid metabolism is recalibrated during bacterial neuroinvasion, and β-hydroxybutyrate promotes the formation and survival of $CD36^+$ foamy macrophages. Altogether, our study uncovers a pathway by which intracellular bacteria hijack macrophages to achieve brain invasion and suggests that lipid metabolism may play a role in the prevention or resolution of bacterial neuroinvasion.

Keywords: intracellular bacteria; neuroinvasion; foamy macrophage; ketogenesis; β-hydroxybutyrate

Introduction

Meningitis is an inflammation of the protective membranes covering the brain that caused by bacterial or viral infection [1,2]. The meninges are composed of multiple layers of membranes, which protect the central nervous system from injury and infection [3,4]. Some bacteria including Salmonella typhimurium (S. typhimurium) and Mycobacterium tuberculosis (M. tuberculosis), can invade the meninges to cause severe brain pathology [5-7]. Bacterial meningitis is a life-threatening infection with extremely high mortality; however, the mechanism by which bacteria invade the brain remains unclear. Efforts to understand the factors that promote neuroinvasion and the host responses to these pathogens are urgently needed.

Phagocytes, such as neutrophils and macrophages, play a predominant role in host responses to the intracellular bacteria [8]. The primary function of phagocytes is to uptake and destroy microorganisms and cell debris through tissue circulation and migration [9,10]. By phagocytosis and antigen presentation, phagocytes act rapidly as the first line of defense against bacterial infections. At the same time, intracellular bacteria can employ sophisticated strategies to replicate within phagocytes and evade host immune surveillance [11-15]. Previous reports have suggested that phagocytes may be hijacked by the pathogens and transport them to the lungs, livers, and kidneys, leading to a risk of dissemination and recurrence [12-14]. Recently, Marc Lecuit and colleagues showed the surface protein InlB of Listeria monocytogenes (L. monocytogenes) protects infected monocytes from immune killing by CD8+ T cells,

thus prolonging the lifespan of infected cells and facilitating the spread of infection to the central nervous system [15]. In this context, phagocytes, especially monocytes/macrophages may play an important part during the brain invasion, but exactly how the intracellular bacteria take advantage of infected macrophages are not well understood.

Infectious diseases and host metabolism are intimately linked. Metabolic signaling has a positive impact on awakening the immune system to resist pathogen invasion. For example, glycolysis bolsters T cell immunity to prevent L. monocytogenes infection [16]. Meanwhile, plenty of studies have shown that bacteria may actively or passively manipulate host metabolites to evade clearance by the host immune system [11,17,18]. Ruminococcus gnavus initiated the biosynthesis of phenethylamine and tryptamine, which exacerbated the progression of diarrhea-predominant irritable bowel syndrome [11]. Legionella pneumophila induces a Warburg-like metabolism by secreting the T4SS effector MitF and decreases oxidative phosphorylation (OXPHOS) in infected macrophages for its survival [17]. Recent report indicates that Nav1.8+ nociceptors send signals to meningeal macrophages via the calcitonin gene-related peptide, and this neuroimmune axis suppresses host defenses and exacerbates bacterial meningitis [18]. These studies imply that there may be a potentially close connection between host metabolism and bacterial brain invasion.

Ketogenesis, induced by fasting or dietary supplementation, is a metabolic pathway

that provides an alternative form of energy for the body and is closely related to the host immune responses [19,20] . Recent report indicates that in pneumonia caused by Pseudomonas aeruginosa, ketone bodies are recycled to the lungs via OXPHOS to maintain airway homeostasis[21]. Consistently, ketogenic diet is reported to activate the expansion of protective γδ T cell responses against influenza virus infection [22]. On the contrary, there is another study reporting that pathogens achieve intracellular survival and infection progression by manipulating the ketogenesis of host. Mice fed a ketogenic diet develop a hyperinflammatory response to systemic lipopolysaccharide and an increased mortality, which is independent of diet-induced microbiota and hyperglycemia [23].Thus, the role of ketogenesis in the progression and migration of infections is controversial [24]. It is well known that β-hydroxybutyrate (BHB) produced by ketogenesis promotes the accumulation of intracellular lipid bodies, serving as both a source of nutrients and a secure niche for intracellular bacteria [25]. However, how ketogenesis/BHB participates in regulating monocytes/macrophages homeostasis and its role in bacterial neuroinvasion is poorly defined.

In this study, we discovered a novel CD36-positive macrophage subpopulation that serves as an immune 'Trojan horse' to cross the blood-brain barrier (BBB) and enable intracellular bacterial neuroinvasion. This macrophage subset has a foamy phenotype, which makes the cells more liable to stay and migrate vertically on the cerebral vascular endothelial surface under the mechanical stress of blood flow. Further, we found that serum BHB, which is possibly derived from ketogenic diet, exacerbates

bacterial neuroinvasion by increasing the formation and promoting the survival of foamy macrophages in peripheral blood. Our study represents a new common strategy of the intracellular bacteria for brain invasion, which could be a potential therapeutic target for the bacterial meningitis.

Result

Foamy macrophage is a potential carrier of bacteria during brain invasion.

To study the role of immune cells in the bacteria neuroinvasion, we performed single-cell RNA-sequencing (scRNA-seq) analyses of peripheral blood mononuclear cells (PBMCs) collected from an acute meningitis model of L. monocytogene infection (Fig.1A). We conducted scRNA-seq at 24 hours post infection, at which timepoint bacteria have massively invaded the brain (Fig.S1A) and the mice began to die (Fig.S1B). Immune cell lineages were identified using canonical surface markers of dendritic cells (DCs: Xcr1, Flt3, CD209a), NK cells (Nkg7), T cells (CD3), monocyte/macrophages (Mo/Mφ: Fcgr1, Adgre1), B cells (CD79), neutrophils (S100a9, S100a8) (Fig.1B-C) [26] . Of these lineages, monocytes/macrophages are involved in phagocytosis and intracellular killing of microorganisms; however, intracellular bacteria could also live in them and migrate to different organs [27,28]. In this case, monocytes/macrophages (n=3535 cells) were extracted and reclustered in silico to precisely delineate subpopulations and their distribution before and after neuroinvasion. Based on differentially expressed cell surface markers and transcripts, we annotated monocytes/macrophages into 6 subpopulations (Fig.1D, S1C). The result showed that the percentage of Cluster 2 cells was sharply increased in the neurolisteriosis group (Fig. S1D). Further, we found that Cluster 2 cells express high levels of genes related to lipid accumulation, including CD36, Pparg , CD9, ApoE, Fabp4 and Trem2 (Fig.1E)[29-33]. This data implied that the functional role of Cluster 2 macrophages is closely related with lipid metabolism. As previously reported, lipid

accumulation in macrophages could easily exceeds their homeostatic capacity, triggering lipid droplet formation and causing the foamy appearance of macrophages [34,35]. To understand the characteristic of Cluster 2 macrophages, $CD36^+$ and $CD36^-$ macrophages were isolated from the peripheral blood by fluorescence-activated cell sorting (FACS). Compared with $CD36^-$ macrophages, the $CD36^+$ subpopulation exhibits significantly higher granularity (SSC^{hi}, Fig.S1E), which is indicative of the amount of proteins or organelles inside and the protrusions on the cell surface. Increased granularity is considered to be one of the characteristics of foamy macrophages [36]. The sorted macrophages were cultured in vitro overnight and then labeled with BODIPY FL, a lipophilic probe for polar and neutral lipids. The result showed that the $CD36^+$ subpopulation accumulated significantly more lipid droplets than the $CD36^-$ macrophages (Fig.S1F). Oil red O staining was also performed to validate this finding (Fig.S1F). To confirm the lipid uptake ability of the $CD36^+$ macrophages, fluorescently labeled Dil-conjugated oxidized low-density lipoprotein (ox-LDL) particles were used and we found that $CD36^+$ macrophages took up more than twice as much ox-LDL as the $CD36^-$ macrophages (Fig.S1H). These data confirmed the foamy appearance of the Cluster 2 macrophages during brain invasion. Then, flow cytometry was performed to detect the percentage changes of foamy macrophages over time during neuroinvasion (Fig.S1E). The result showed that the percentage of $CD36^+$ foamy macrophages in peripheral blood steadily increased over time during neuroinvasion (Fig. 1F). Among all macrophages, the percentage of $CD36^+$ subgroup can reach up to more than 52% (Fig. 1G). In addition, the percentage

of foamy macrophages in the peripheral blood were positively associated with the bacterial load in the brain (Fig.1H). These data implied that $CD36^+$ foamy macrophages may be involved in the bacteria neuroinvasion. Furthermore, immunofluorescence co-localization analysis was used to validate this hypothesis. The results showed that the number of foamy macrophages attached to the vascular endothelial cells increased as neuroinvasion progressed in the acute meningitis model (Fig.1I). Taken together, these results suggest that $CD36^+$ foamy macrophage may play an important role during bacterial brain invasion.

Foamy macrophage facilitates intracellular bacteria across the blood-brain barrier both in vitro and vivo.

Next, we seek to understand the necessity of $CD36^+$ foamy macrophages in the bacterial neuroinvasion. We constructed an in vitro BBB model based on the Transwell system using mouse primary brain vascular endothelial cells and neurons (Fig.2A). It has been reported that ox-LDL induces foamy cell formation by enhancing CD36 expression [37]; therefore, peritoneal macrophages isolated from mouse were converted into foamy macrophages by treating with different concentrations of ox-LDL for 24 h (Fig.S2A). Subsequently, macrophages were infected with L. monocytogene (MOI=10) and then inoculated to the upper chamber of the BBB model. It was confirmed that intracellular bacteria load was increased with the transformation of foamy macrophages (Fig.S2B). Notably, the number of L. monocytogene crossing the barrier was significantly increased with the assistant of

ox-LDL stimulated macrophages, and foamy macrophages facilitated this invasion in a dose dependent manner (Fig.2B).

To understand whether the increasing of foamy macrophage favors the transfer of L. monocytogenes into the brain in vivo, we performed macrophage transfusion experiments through tail vein injection based on the cyclophosphamide (CTX)-induced immunodeficient mouse model. After recovery from CTX treatment for 12 hours, mice were infected with L. monocytogenes, and 18 h later samples were collected for further examinations (Fig.2C). In consistent with previous studies, L. monocytogene-induced clinical phenotype and mortality were relieved by transfusion of purified peritoneal macrophages [38,39] (Fig. 2D, S2C-D). However, the body weight was reduced (Fig. S2C), the comprehensive clinical scoring was increased (Fig. S2D), and the survival time (Fig. 2D) was shortened in mice with transfusion of ox-LDL stimulated macrophages when compared with control. Further, we showed that the bacterial loads of brains in the mice transferred with foamy macrophages were significantly higher than that transferred with purified peritoneal macrophages (Fig.2E). Interestingly, the bacterial loads did not differ in the lungs, spleens, and livers (Fig. S2E). We also tested the proinflammatory factor levels in the plasma and brain homogenate. The results showed that IL-6 and TNF-α were remarkably increased in the foamy macrophage-transferred mice (Fig.2F-G), indicating a more severe meningitis phenotype in the foamy macrophage-transferred group. The pathological histology analysis confirmed that there were more severe inflammation and neuron damage in the cerebral cortex of foamy macrophage-transferred mice than

the control (Fig.S2F-G). In addition, when mice were infected with a relatively low-dose (5×10^7 CFU per mouse) of L. monocytogenes, the difference in bacterial load in brain tissues between foamy macrophage-transferred and the control group was even greater than that under high dose condition (Fig.S2H-I). These data suggest that foamy macrophages-mediated neuroinvasion is not restricted to high-dose bacteria induced acute meningitis model.

Foamy macrophage is an optimum niche supporting the nutrition and persistence of intracellular bacteria [40]. We then asked whether the role of foamy macrophage during brain invasion apply to other intracellular bacteria. Firstly, the positive correlation between foamy macrophage and neuroinvasion was observed in the meningitis models of intracellular bacteria S. typhimurium (Fig.S3A-B), as well as the Methicillin-resistant Staphylococcus aureus (MRSA) (Fig.S3C-D), which, although not a classical intracellular pathogen, has significant intracellular habitation[41]; however, this finding was not validated in the extracellular bacteria S. pneumoniae infection model (Fig.S3E-F). Then, macrophage transfusion experiments were performed to further verify the carrier role of foamy macrophages in the intracellular bacterial invasion of the brain. The results showed that the differences of CFU load in brain tissues between foamy macrophage-transferred and control groups were still observed in the intracellular habitation bacteria MRSA (Fig.S3G-K) meningitis models, but not in the S. pneumoniae infection models (Fig.S3L-O). Together, these data suggest that foamy macrophages greatly contribute to the process of intracellular bacterial neuroinvasion.

PCSK9 (proprotein convertase subtilisin/kexin 9) belongs to a proprotein convertase family, which plays a role in cholesterol and fatty acid metabolism [42,43] . The intracellular LDL-cholesterol level is accumulated through protecting LDL receptor (LDLR) from degradation in PCSK9$^{-/-}$ mice [44,45] . We showed that PCSK9$^{-/-}$ mice had significantly higher content of lipid (Fig.S4A-B) and higher percentage of CD36^{+} foamy macrophages (Fig.S4C) in the peritoneal blood than their littermates, and there were more L. monocytogene parasitizing in the PCSK9$^{-/-}$ macrophages compared with that in WT cells after infection (Fig.S4D). Therefore, we used PCSK9$^{-/-}$ mice as a model of spontaneously formed foamy macrophages to verify the reliability of our findings by macrophage transplantation experiments. After recovery from transplantation for 12 hours, mice were intraperitoneal injected with 2×10^{8} CFU of L. monocytogenes, and 12 hours later samples were collected for further examinations (Fig.2H). We found that the brain bacterial loads were significantly higher in the WT recipients which had received transplantation of PCSK9$^{-/-}$ macrophages than those that had received control macrophages (Fig.2I). Similar results were observed in the knockout recipients (Fig.2I). However, differences in CFU load were only manifested in brain tissues and not in other organs such as lungs, spleens, and livers (Fig. S4E). Consistently, the mortality (Fig.2J), and proinflammatory factors in the plasma (Fig. S4F) and brain homogenate (Fig. S4G) were aggravated in both WT and knockout recipients by transplantation of PCSK9$^{-/-}$ macrophages. Since L. monocytogene is a food-borne pathogen that can invade the body through the gastrointestinal tract, this finding was further confirmed by oral administration of L. monocytogenes in the

same experimental model (Fig.2K-L, S4H-J). Taken together, these data indicate that excess lipid accumulation contributes to the foamy appearance of macrophages, thus facilitating the neuroinvasion of intracellular bacteria.

Fluid Mechanics indicate the increased adhesion and resistance of foamy cells during the neuroinvasion.

We next asked how foamy macrophages exploit their properties to accumulate on the cerebral blood vessel wall and participate to the process of intracellular bacterial neuroinvasion. We applied a two-dimensional live-cell flow chamber assay by microfluidic chip to decipher the multistep process of macrophages on the surface of vascular endothelium under physiological flow (Fig.3A). Adhesion ability was calculated by counting the cumulative number of macrophages adhering to the endothelial monolayer under a certain shear stress. We found that with the increase of the percentage of foamy macrophages, the number of cells adhering to the endothelial monolayer also increased (Fig.3B-C). Because adherent cells could be detached with the increase of shear stress, we tested the dynamics of the shear resistance of foamy macrophages. The results showed that the shear resistance of foamy macrophages was significantly stronger than that of the control macrophages, and they performed outstandingly in resisting high shear stress (Fig.3D). Further, we investigated the effect of endothelial density on the performance of macrophage adhesion. It was showed that the cell density, rather than the cell type, of endothelium had a great impact on the adhesion, and foamy macrophages tended to adhere to the surface of

dense endothelial cells (Fig.S5A-D).

Once being attached on endothelium monolayer, macrophage will crawl along the monolayer and find a location to cross the endothelium monolayer in the presence of blood flow [46,47]. We next tested the performance of foamy macrophages in post-arrest crawling on endothelium monolayer. We acquired sequential images of macrophages at a shear stress of 2 dyne/cm^2 and then analyzed them by defining various parameters of crawling dynamics (Fig.S5E). The observations were presented by crawling trajectories of individual cell (Fig.3E), and we found that the crawling ability of adherent foamy macrophages was dampened, reflecting in shortened crawling displacement and slowed down crawling speed (Fig.3F-G). However, there was no obvious differences among the crawling duration (Fig.S5F). Furthermore, directionality is also critical for representing cell crawling dynamics, which is quantified as the ratio of displacement along shear flow to the perpendicular. The result showed that the directness of macrophages was slightly but significantly enhanced with the stimulation of 80 μg/mL ox-LDL, implying that the existence of lipid droplet preferred to intentionalize cell crawling towards vertical direction (Fig.3H). We also compared a key dynamic parameter of transmigrating duration, which is defined as the interval from the time point of cell arrival at site to the endpoint of completion of transmigration underneath endothelium monolayer (Fig.S5G). The result showed that the transmigration duration was significantly shortened in the foamy macrophage groups (Fig.3I).

Considering that protrusion is critical for cell crawling and migration, we then

investigated whether the intercellular lipid could affect the formation of protrusion. The results showed that the number, as well as the length of protrusion were significantly increased in the macrophages with ox-LDL stimulation (Fig.3J-K). We further quantified the cell area of macrophage and found that the area of single cell was larger under ox-LDL stimulation (Fig.3L). Additionally, we examined various integrins and adhesive ligands expressing on the cell surface, which have been reported to be involved in adhesion and migration [48]. The result showed that the expression levels of α-integrins, β-integrins and intercellular adhesion molecules were significantly upregulated by ox-LDL treatment (Fig.3M). Collectively, these data suggest that the foaming of macrophages greatly enhances their adhesion under mechanical stress, predisposing them to stay and migrate vertically on the cerebral vascular endothelial surface, which may be attributable to the formation of protrusions as well as the expression of integrins and adhesion ligands.

β-hydroxybutyrate promotes the foamy macrophage and exacerbates neuroinvasion via the HCAR2 receptor.

Since the foamy appearance is closely linked to the excess lipid accumulation in macrophages, lipid metabolomics analysis of serum samples was performed to uncover the formation of foamy macrophages during bacterial neuroinvasion. Principal component analysis (PCA) revealed that distinct metabolite genotype clusters were generated in the neurolisteriosis group (Fig.4A). The volcano plot indicated that 70 fatty acids (FAs) were upregulated and 71 FAs were downregulated

(p<0.05, |log2FC|>1) in the neurolisteriosis group. (Fig.4B, Table S2). The 70 upregulated FAs were classified into four subclusters according to the number of carbon atoms in the alkyl chain length, and we found that BHB, which has been reported to favor the foamy phenotype of macrophages [49], was the only short-chain fatty acid among all the upregulated FAs (Fig. 4C). KEGG-based analysis revealed that metabolites related to the synthesis and degradation of ketone bodies were enriched (Fig. S6A), and metabolomics data showed that (R)-3-hydroxybutanoate was significantly increased during neuroinvasion (Fig. S6B). Based on these data, we detected the level of serum BHB in the acute meningitis model of L. monocytogene infection. The result showed that the BHB level climbed steadily over time and then decreased lightly (Fig.4D). Consistently, an upregulation of genes controlling ketogenic enzymes (HMGCS2 and CPT1A) in the liver was observed as infection persists (Fig.S6C-D). Meanwhile, mice experienced weight loss and decreased appetite during the experiments, which is partly related to the enhanced ketogenic ability after infection (Fig.S6E-F). Further, steady increase of serum BHB was also observed in the meningitis models caused by MRSA and S. typhimurium (Fig.S6G-H). These data confirm that the production of BHB is significantly induced during bacterial neuroinvasion.

As previously reported, BHB promotes the foamy phenotype of macrophages via the hydroxycarboxylic acid receptor 2 (HCAR2) receptor [25]. Next, HCAR2 knockout mice were used to study whether BHB can promote bacterial infection in the brain. We confirmed that lipid droplet accumulation and CD36 expression in macrophages

were all increased dramatically upon BHB stimulation, and there was no significant difference when HCAR2 was knocked out (Fig.4E-G). BHB inhibits adenylyl cyclase activity through the HCAR2 receptor and reduces cellular cAMP levels, thereby protecting lipid droplets from lipolysis by hormone-sensitive lipases [25]. Therefore, we used cAMP (1mM) to test this theory. As a result, pretreatment of cAMP restored the increase in lipid content and intercellular bacterial burden stimulated by BHB; however, this phenomenon was not found in HCAR2$^{-/-}$ macrophages (Fig. S6I-J). By using the in vitro BBB model (Fig.2A), the number of bacteria crossing the barrier increased significantly in response to BHB stimulation in controls, but not in HCAR2$^{-/-}$ macrophages (Fig.4H). Further, peritoneal macrophages of WT and HCAR2$^{-/-}$ mice were isolated to further assess the effects of BHB on the biophysical dynamics of macrophages. The data demonstrated that BHB significantly altered the static or shear resistant adhesion of control cells instead of HCAR2$^{-/-}$ macrophages (Fig. 4I-K). Meanwhile, we showed that BHB greatly impaired the crawling ability of macrophages, including shortened crawling displacement, slowed down crawling speed and unpredictable directness (Fig. 4L-O). In addition, the transmigrating ability of the macrophages was significantly decreased when the cells were pretreated with BHB (Fig. 4P). Consistently, the expression levels of α integrin family were significantly upregulated by BHB treatment in wild type but not HCAR2$^{-/-}$ macrophages (Fig. 4Q). These data collectively indicate that BHB facilitates the foamy phenotype of macrophages through the HCAR2 receptor, thus affecting the process of bacterial neuroinvasion.

β-hydroxybutyrate promotes the survival of macrophage via HCAR2-mediated calcium influx.

Foamy stage appears to be a terminal point of macrophage differentiation[50], we asked whether, in addition to converting peritoneal macrophages into the foamy phenotype, cell survival also contributes to the increase in the absolute quantity of foamy macrophages induced by BHB treatment. It was showed that LDH-activity in the culture medium was significantly reduced in response to BHB treatment, indicating a decrease in cell death (Fig.5A). Propidium iodide (PI) staining was used to evaluate the membrane integrity of L. monocytogene-infected macrophages, we found that PI positive cells was decreased from 59.7% to 24.5% under BHB stimulation, and there was no significant difference in cell viability between BHB treatment and control group when HCAR2 was knocked out (Fig. 5B-C). Calcium influx is generally recognized to be a signal that triggers cell membrane repair[51]. To investigate the impact of BHB-HCAR2 signaling on cytosolic calcium concentration, infected macrophages were loaded with Fluo-4 AM, a fluorescent $Ca2^{+}$ indicator. The result showed that BHB induced a remarkable intracellular calcium accumulation, and HCAR2 knockdown eliminated the calcium influx in macrophages (Fig.5D). Pretreatment of macrophages with BAPTA-AM, a Ca2+ chelator, reversed the BHB-induced increase in cell survival (Fig.5E-F). Further, we tested whether calcium flux is associated with foamy macrophage-mediated intracellular bacterial penetration of the BBB. As a result, inhibition of calcium flux had no impact on the bacterial uptake

by macrophages in the upper chamber (Fig. S7A); however, differences in the CFU loads were observed in the macrophages that had crossed the barrier (Fig. 5G). We next investigated how BHB maintains the survival of foamy macrophage. As previously reported that calcium influx initiates membrane repair mainly through recruitment of the endosomal sorting complexes required for transport (ESCRT) machinery[52]. Our data showed that BHB treatment significantly increased the number of CHMP4-positive puncta, which indicates the assembly of ESCRT in the infected macrophages, and this membrane repair process could be blocked by HCAR2 knockdown or BAPTA-AM treatment (Fig.5H-I, S7B-C). In addition, cellular membrane repair also relies on lysosomes, which can rapidly fuse with the plasma membrane when intracellular $Ca2^{+}$ concentration rises. Therefore, we examined lysosomal exocytosis in the infected macrophages by exofacial LAMP1 and the release of lysosomal enzymes, such as acid phosphatase (ACP), β-galactosidase (β-gal) and β-hexosaminidase (β-hex). The results confirmed that BHB promoted the lysosomal exocytosis in the infected macrophages through the HCAR2 receptor (Fig.5J-L, S6D-F). These data collectively indicate that BHB signaling activates Ca^{2+}-mediated membrane repair, thereby keeping the survival of foamy macrophage via HCAR2 receptor.

Ketogenesis exacerbates intracellular bacterial neuroinvasion.

BHB can be synthesized via the metabolism of fatty acids and ketogenesis [53]. To understand the relationship between ketogenesis and bacterial meningitis, mice were

given different doses of ketone ester drink for 4 weeks, and then infected with L. monocytogenes by intraperitoneally injection (Fig. 6A). The data illustrated that ketone ester drinking elevated the levels of serum BHB (Fig. 6B), accompanied by remarkable increases in the clinical scores (Fig. S8A), mice mortality (Fig. 6B) and bacterial load in brain tissues (Fig. 6D). Dietary modulation can increase and maintain circulating metabolites in human circulation, and accumulating data demonstrate that ketogenic diet elevates the level of BHB [54]. Ketogenic diet is a low-carb, high-fat diet that causes weight loss and provides numerous health benefits, including alleviating symptoms of neurodegenerative diseases, cardiovascular diseases, and cancers [55-58] . We next asked whether ketogenic diet is associated with bacterial neuroinvasion. HCAR2$^{-/-}$ mice and their littermates were given normal or ketogenic diet for four weeks respectively, then mice were infected with L. monocytogenes by intraperitoneally injection (Fig.6E). As a result, the lifespan of HCAR2$^{+/+}$ mice fed a ketogenic diet was significantly shortened under L. monocytogene infection, and the survival disadvantage caused by dietary modulation was abrogated by HCAR2 knockout (Fig.6F). Consistently, the clinical scores (Fig.S8B), the percentage of foamy macrophages in peritoneal blood (Fig.6G), the intracellular bacterial burden of the macrophages (Fig.6H), and the CFU loads in the brain tissues (Fig.6I) were all greatly increased in the HCAR2$^{+/+}$ mice with ketogenic diet. Interestingly, mice in the ketogenic diet group owned less weight loss than the control group (Fig.S8C), and more bacteria were observed to spread to other organs in the ketogenic diet mice (Fig.6I). Further, the proinflammatory factors levels in plasma and brain homogenate

were also examined. The results showed that, ketogenic diet induced a significant increase in proinflammatory cytokine levels (Fig.8J-K) and more severe neuronal damage (Fig.8L-M) in wild-type mice, while it had no effect on the HCAR2$^{-/-}$ mice. These data were confirmed by oral administration of L. monocytogenes in the same experimental model (Fig.S8D-G). Additionally, we used MRSA, another type of intracellular bacteria, to further verify our findings. The data indicated that, as expected, a ketogenic diet promoted the brain invasion of MRSA and exacerbated symptoms of meningitis (Fig.S8H-J). Taken together, our data show that the ketogenic diet may exacerbate bacterial neuroinvasion and hasten the demise of mouse, primarily depending on the elevated serum BHB via HCAR2 receptor.

Serum β-hydroxybutyrate fuels the symptoms during the human bacterial meningitis.

Our data thus far suggest that BHB-induced foamy macrophages play an important role in the bacterial neuroinvasion in mice. Next, we sought to assess whether the accumulation of foamy macrophages or BHB could also be identified and are associated with the bacterial meningitis in human samples. Gender and age-matched tubercular meningitis subjects (n=62) and healthy individuals (n=60) were recruited and peripheral blood samples were collected for analysis (Fig 7A). There were no significant differences in blood glucose and insulin concentrations between the two groups (Fig. S9A, C), and there was no correlation between these parameters and BHB levels (Fig. S9B, D), thus excluding the involvement of glucose and insulin in

the differential production of BHB. As a result, serum BHB levels were significantly elevated in the meningitis patients compared with healthy control individuals, suggesting an infection-induced ketogenesis (Fig 7B). Interestingly, compared with the healthy controls, serum cholesterol levels, including total cholesterol (TC) and low-density lipoprotein cholesterol (LDL-C) were increased in the patients, while high-density lipoprotein cholesterol (HDL-C) were slightly but not significant reduced (Fig S9E-G). To investigate whether the BHB is associated the severity of infection, the patient individuals were further divided into three groups, high (BHB level at the top 1/3 among the samples tested, n=21), moderate (middle 1/3, n=20) and low (bottom 1/3, n=21), based on BHB levels (Fig 7A). Clearly, patients with high BHB levels exhibited higher clinical scores than patients with low BHB levels (Fig 7C). Consistently, BHB high patients had higher cell accounts (Fig 7D) and protein (Fig 7E) in the cerebrospinal fluid, higher indication of infection indexes (Fig. 7F, WBC; Fig. 7G, PCT), as well as higher markers of inflammatory conditions (Fig. 7H, ESR; Fig. 7I, CRP), suggesting increased disease severity. These data implied that infection-induced ketogenesis may be an important fuel in severe bacterial neuroinvasion.

To explore the dynamic of foamy macrophages and BHB in the pathogenesis of bacterial meningitis, individuals were followed during hospitalization. We found that foamy macrophages and BHB levels in patients tended to increase during the disease progression stage, and decreased during the recovery stage (Fig 7J-K). To further confirm the relationship between foamy macrophages and bacterial meningitis

pathology, PBMCs of patients or healthy controls were collected for analysis. We found that compared with healthy controls, the expression of genes involved in cholesterol uptake were significantly heightened (Fig 7L), while the genes related to cholesterol utilization and excretion were reduced in macrophages of meningitis patients (Fig 7L). Together, these data indicate that BHB fuels human bacterial meningitis through promoting the development of the foamy macrophage.

Discussion

Our findings suggest that foamy macrophages serve as a carrier for bacterial colonization in the brain, facilitating the penetration of intracellular bacteria across the BBB. Also, we found that BHB level experiences a significant increase in the peripheral blood of meningitis patients. Mechanistically, BHB regulates the dynamics and morphological changes of foamy macrophages and promotes the cell survival by activating HCAR2 receptor, which is a key signaling in the neuroinvasion of intracellular bacteria. Furthermore, under ketogenic diet conditions, elevated BHB levels promote the formation of foamy macrophages, thereby exacerbating bacterial transport to the brain.

Normally, the BBB prevents bacteria or viruses from crossing unless there is significant trauma to the brain. However, specific bacteria can penetrate the BBB through their unique mechanisms and cause severe brain infections [1,15]. For example, Streptococcus pneumonia colocalizes with the endothelial receptors polymeric immunoglobulin receptor (pIgR) and platelet endothelial cell adhesion molecule

(PECAM-1), leading to brain invasion. Streptococcus agalactiae enhances pro-inflammatory cytokines and intercellular adhesion molecule 1 production from endothelial cells via activation of the inducible nitric oxide synthase (iNOS) pathway, resulting in the direct BBB disruption[1]. For the intracellular bacteria, Listeria InlB is reported to protect infected monocytes from Fas-mediated cell death by $CD8^+$ T cells and extend the lifespan of infected monocytes[15]; M. tuberculosis may protect infected cells from cell death, thus promoting their survival and neuroinvasion[59]. In this context, it is likely that the intracellular bacteria may utilize the host's cells, especially immune cells, to achieve brain invasion. In this study, we identify foamy macrophages can be hijacked by intracellular bacteria and serve as vehicles for the invasion of the BBB. Foamy macrophages tend to have more protrusions and a larger cell area, which make the cells more conducive to colonization on vascular endothelial walls under the pressure of blood flow.

Pathogens may exploit most of the host's nutrients, including glucose, glycerol, fatty acids, N-acetylglucosamine (GlcNAc), and several other carbon substances for invasive transmission[60]. The SPI-1 effector SopE2 of S. Typhimurium utilizes accumulated glycolytic intermediates as carbon sources, leading to the intracellular replication and pathogenicity[61]. Our findings demonstrate that intracellular bacteria can actively influence host free fatty acid metabolism (Fig.4A-C) and manage to reprogram macrophages, thereby exacerbating neuroinvasion. Foamy macrophages are formed through dysregulation of lipid metabolism. The formation of foamy

macrophages impairs the immune function of macrophages and contributes to pathogenesis. For example, foamy macrophages play a key role in the initiation, progression, and instability of atherosclerosis [62,63]. In multiple sclerosis, myelin-laden foamy macrophages in brain lesions are associated with demyelinating activity and chronic active lesions[64]. During tuberculosis, death by foamy macrophage necrosis expands tuberculous lesions in the lung parenchyma, causing progressive destruction of lung tissue and loss of lung function in patients with active tuberculosis[65]. In this study, we discover that BHB derived from a ketogenic diet promotes the formation of foamy macrophages in peripheral blood, thus facilitating bacterial neuroinvasion. Interestingly, we found that serum cholesterol levels, including TC and LDL-C were significantly higher in the meningitis patients when compared with the healthy controls (Fig.S9E, G). We hypothesize that cholesterol or other lipid metabolites may also contribute to the formation of foamy macrophages. However, this hypothesis needs to be verified further experimentally.

Biomechanical data indicate that foamy macrophages adhere more strongly to endothelial surface than normal macrophages, and that this adhesion-enhancing effect is more pronounced when the endothelial cells are dense (Fig.3B-C). This suggests that foamy macrophage-mediated bacterial invasion affects the brain to a greater extent than other tissues. Based on this, we show that the increase of foamy macrophages in peripheral blood leads to the transfer of bacteria mainly to the brain, rather than to other organs (Fig3, FigS5). However, we found that ketogenic diet and

ketone ester supplementation significantly increase the bacterial load in the brain and other tissues such as liver and lung (Fig6), suggesting that ketogenesis, in addition to promoting foamy macrophage generation, may have other unknown roles in the intracellular bacterial infections. Therefore, the role of ketogenesis in the formation of foamy macrophages and the contribution of ketogenesis in the bacterial neuroinvasion should be further determined.

The basal metabolic status of the host may also have a great influence of the bacterial neuroinvasion through modifying immune cells. Previous study has found that cardiac endothelial cells can oxidize ketone bodies and promote cell proliferation, migration, and blood vessel sprouting [66]. Increasing ketone body levels with a ketogenic diet increases endothelial cell proliferation and prevents vascular rarefication in hypertrophied mice model[66]. It is unclear whether ketogenesis directly affects the development or permeability of the BBB, leading to an increase in bacterial invasion. Meanwhile, our study found that mice experienced weight loss and decreased appetite during the experiments (Fig.S6E-F), which was also observed in COVID-19 infection[67]. Therefore, we are currently unable to determine whether elevated BHB levels are caused directly by pathogenic bacteria or by hepatic ketogenesis.

This study demonstrates that a BHB-rich environment created by the ketogenic diet renders mice more susceptible to L. monocytogene-induced neuroinvasion. Mechanistically, BHB prevents foamy macrophages from senescence via HCAR2-mediated membrane repair. However, inhibition of HCAR2 signaling or calcium influx reverses the increase in foamy macrophage survival but does not completely

reverse the increase in bacterial neuroinvasion induced by BHB (Fig.5E-F). These data suggest that BHB-induced bacterial brain invasion is not solely dependent on calcium influx and that other potential mechanisms may also be involved in this process. However, this hypothesis needs to be verified further experimentally.

Acknowledgments

This work was supported by the National Natural Science Foundation of China (No. 92369115), the Fundamental Research Funds for the Central Universities (No. 2023CDJXY-009 and 2019CDYGZD009), Natural Science Foundation of Chongqing, China (No. CSTB2023NSCQMSX0402), and Chongqing Talents: Exceptional Young Talents Project (No. cstc2021ycjh-bgzxm0099). The funders had no role in study design, data collection and analysis, decision to publish, or preparation of the manuscript.

Author Contributions

H.W., Q.Z., X.M., X.L. and Z.S. conceived and designed the study. Z.S., H.Y., H.F., Q.H., B.F., Y.X. and D.G. performed the animal experiments. Z.S., K.Y., Q.H., Q.L., Y.D. and X.Z. carried out healthy volunteer and patient recruitment and sample collection. Z.S., N.L. and X.S. carried out the live-cell flow chamber assays. H.W., Z.S., K.Y., H.Y. and X.Z. collected and analyzed the data. X.T., S.F., J. L., R.Y., W.G., X.M. and M.L. contributed to experimental material and insightful suggestions. H.W.,

X.L., X.Z. and Z.S. wrote the manuscript. H.W. and Q.Z. coordinated the project. All authors read and approved the final manuscript.

Declaration of interests

The authors declare no competing interests.

Figure Legends

Figure 1. Identification of foamy macrophage accumulation during the L. monocytogene neuroinvasion.

(A) Experimental design summary (n=5 control mice and n=7 mice with L. monocytogene in 24h).

(B) UMAP representation of integrated transcriptome-based clustering of 17351 total PBMCs with identification of the major immune cell lineages.

(C) Dot plot showing expression of the selected transcripts in immune cells clusters. All the transcripts shown significantly enriched in the relevant clusters with adjusted P-value <0.05.

(D) Cells corresponding to monocytes and macrophages were extracted for reclustering and tSNE dimensional reduction analysis with annotated cell clusters.

(E) Transcript expression projected onto the tSNE plot for CD36, Pparg, Fabp4, CD9, ApoE and Trem2 and used to identify and annotate clusters.

(F-G) Flow cytometry of the percentage of the $CD36^+$ foamy macrophages among PBMCs (F) and total macrophages (G) during the neurolisteriosis separately. Experiments were performed in triplicate. Data are presented as the mean ± SEM. *p < 0.05.**p < 0.01.

(H) Correlation between the percentage of the $CD36^+$ foamy macrophages and the bacterial burdens in brains during the neuroinvasion. The p value was calculated using Spearman's test. R, spearman correlation coefficient.

(I) Immunofluorescence staining of foamy macrophages accumulation in the cerebral vascular during the neuroinvasion. Macrophages were stained with CD11b (red) and lipid droplets were stained with BODIPY493/503 (green). The boundary of vascular was shown as dashed lines. Scale bar, 100 μm.

Figure 2. Infected foamy macrophages transfer bacteria to invade the brain parenchyma both in vitro and vivo.

(A-B) (A) Schematic diagram of in vitro BBB model based on Transwell system. Macrophages pretreated with different concentration of ox-LDL were challenged with L. monocytogenes (MOI = 10) for 2 h. The infected macrophages (5×10^4 cells/well) were added into the upper chamber. The conventional incubation time was 12h and then the neurons cells in the bottom chamber were lysed for penetrating bacterial quantification. (B) The number of penetrating bacteria were quantified.

(C) Experimental diagram of macrophages transplantation and infection in wild type mice. Purified peritoneal macrophages with or without ox-LDL stimulation were infused into CTX-pretreated mice before bacterial infection.

(D-G) (D) Survival rate of mice after L. m infection (n=10 for each group). (E) Bacterial burdens in brains from mice on day 1.25 after intraperitoneal infection with 2×10^8 CFU L. m (n=5 for each group). (F-G) Cytokine levels of plasma (F) and brain homogenate (G).

(H) Schematic diagram of macrophage transplantation and infection experiment in $PCSK9^{+/+}$ (WT) and $PCSK9^{-/-}$ (KO) mice. Peritoneal macrophages from $PCSK9^{+/+}$

and PCSK9$^{-/-}$ mice were injected into PCSK9$^{+/+}$ and PCSK9$^{-/-}$ mice separately before L. monocytogene infection.

(I-J) (I) Bacterial burdens in brains from mice on day 1.5 after intraperitoneal infection with 2×10^8 CFU L. m (n=5 for each group). (J) Survival rate of mice after L. m infection (n=10 for each group).

(K-L) (K) Bacterial burdens in brains from mice on day 1.5 after oral administration with 2×10^8 CFU L. m (n=5 for each group). (L) Survival rate of mice after L. m infection (n=10 for each group).

Experiments were performed in triplicate. Data are presented as the mean ± SEM. *$p < 0.05$.**$p < 0.01$. Abbreviation: ns, nonsignificant.

Figure. 3 Two-dimensional live-cell flow chamber assays of the movement characteristics of infected foamy macrophages.

(A) Schematic diagram of live-cell flow chamber experiment.

(B-C) (B) Optical images of infected macrophages adhesion on the surface of monolayer endothelial cells under different concentrations of ox-LDL. Scale bar, 200 μm. (C) Adherent cell count in each field of view were quantified.

(D) After macrophages having adhered on the endothelial cells at 1 dyne/cm2 for 30 min, the stress was stepwise increased to 2, 4, 8, 16, and 32 dyne/cm2 for 30 s each to detach those adhered cells.

Normalized adhesion fraction was plotted for resting control and ox-LDL stimulation.

(E-H) Crawling dynamics of macrophages under different concentrations of ox-LDL

on the monolayer endothelial cells under flow. (E) Typical trajectories of infected macrophages crawling on monolayer endothelial cells. For each trajectory, the arrested sites of macrophages were overlaid at the origin of the diagram (x/y=0/0) and the corresponding end points were indicated with dots. Arrows indicate the flow direction. Normalized crawling displacement (F), velocity (G) and directness (H) were quantified (n=8).

(I) Transmigration duration of macrophages after securely adhering on the surface of monolayer endothelial cells.

(J-K) (J) The number and (K) mean length of protrusion in the infected macrophage under different concentrations of ox-LDL were quantified (n=10).

(L) The area of infected macrophages under different concentrations of ox-LDL were quantified (n=30).

(M) Heatmap of intercellular adhesion molecules among macrophages.

Experiments were performed in triplicate. Data are presented as the mean ± SEM. *$p < 0.05$.**$p < 0.01$. Abbreviation: ns, nonsignificant.

Figure 4. β-hydroxybutyrate aggravates bacterial neuroinvasion by promoting the formation of foamy macrophages via the HCAR2 receptor.

(A-C) Lipid metabolomic profiling analyses of serum from the mice with neurolisteriosis and the control (n=7). (A) Principal coordinates analysis (PCA) analysis of the group difference. (B) Volcano plot of differential fatty acids. (C) Pie chart of the number of up-regulated FAs (SCFA, exercise fatty acids; MCFA, medium

chain fatty acid; LCFA, long chain fatty acids; VLCFA, very long chain fatty acid).

(D) Heatmap of dynamics of serum BHB levels in mice during the neuroinvasion.

(E-P) Peritoneal macrophages from 8-week-old HCAR2$^{+/+}$ and HCAR2$^{-/-}$ mice were prepared for functional analysis.

(E-F) (E) Flow cytometry of BODYPY FL in the macrophages with BHB (0, 5, 10 mM) for 24h. (F) MFI was quantified.

(G) Flow cytometry of percentage of CD36^{+} foamy macrophages with BHB (0, 5, 10 mM) for 24h.

(H) The number of penetrating bacteria with the assistance of infected HCAR2$^{+/+}$ and HCAR2$^{-/-}$ macrophages with BHB (10mM) for 24h. ox-LDL was used as positive control.

(I-K) HCAR2+/+ and HCAR2-/- macrophages were pretreated with BHB (10mM) for 24h and then infected with L. m (MOI=10). (I) Optical images of adherent macrophages on the surface of monolayer endothelial cells. Scale bar, 200 μm. (J) Adherent cell count in each field of view were quantified. (K) Normalized adhesion fraction of HCAR2$^{+/+}$ and HCAR2$^{-/-}$ macrophages with BHB (10mM) adhesion were plotted.

(L-P) Crawling and migrating dynamics of infected HCAR2$^{+/+}$ and HCAR2$^{-/-}$ macrophages with BHB (10mM) on the monolayer endothelial cells under flow. (L) Typical trajectories of infected macrophages crawling on monolayer endothelial cells. Normalized crawling displacement (M), velocity (N), directness (O) and transmigration duration (P) were quantified (n=8).

(Q) mRNA expression of intercellular α intergrin among the infected HCAR2+/+ and HCAR2-/- macrophages.

Experiments were performed in triplicate. Data are presented as the mean ± SEM. *p < 0.05.**p < 0.01. Abbreviation: ns, nonsignificant.

Figure 5. β-hydroxybutyrate promotes the survival of macrophage via HCAR2-mediated calcium influx.

(A-C) HCAR2$^{+/+}$ and HCAR2$^{-/-}$ macrophages were pretreated with BHB (10mM) for 24h and then infected with L. m (MOI=10). (A) Percentage of released lactate dehydrogenase (LDH) in the cell culture medium. (B) Immunofluorescence of macrophage stained for Propylene glycol (PI). DAPI (blue) marks the nucleus and PI (red) marks the cell membrane. (C) Percentage of PI^{+} cells were quantified.

(D) Flow cytometry of intracellular calcium concentration in infected HCAR2$^{+/+}$ and HCAR2-/- macrophages are loaded with Fluo-4 AM (a fluorescent Ca^{2+} indicator), and BHB (10mM) would be added after 30 seconds.

(E-G) HCAR2$^{+/+}$ and HCAR2$^{-/-}$ macrophages were pretreated with BHB (10mM) and BAPTA-AM (10 mM) for 24h and then infected with L. m (MOI=10). (E)Percentage of PI+ cells were quantified. (F) Percentage of released lactate dehydrogenase (LDH) in the cell culture medium. (G) The number of penetrating bacteria in the lower chamber were detected in 12 and 24h.

(H-I) (H) Time-lapse confocal images of CHMP4-GFP-expressing in the infected HCAR2$^{+/+}$ and HCAR2$^{-/-}$ macrophages with BHB (10mM) for 0, 5, 10, 15, 20, 30 min.

(I) CHMP4-GFP puncta were quantified.

(J-L) HCAR2$^{+/+}$ and HCAR2$^{-/-}$ macrophages were pretreated with BHB (10mM) for 24h and then infected with L. m (MOI=10). (J) Flow cytometry of LAMP1 expression on the cell surface. (K) Normalized MFI was quantified. (L). Percentage of released acid phosphatase (ACP), β-galactosidase (β-gal) and β-hexosaminidase (β-hex) activity in the cell culture medium.

Experiments were performed in triplicate. Data are presented as the mean ± SEM. *$p < 0.05$.**$p < 0.01$. Abbreviation: ns, nonsignificant.

Figure 6. Ketogenesis exacerbates L. monocytogene-induced neuroinvasion.

(A-C) (A)Ketone ester (10, 20 mg/ml) were added in the drinking water for 2 weeks and then C57BL/6 mice were challenged with 2×10^8 CFU L. m (n=5 for each group). (B) Serum BHB levels; (C) Survival rate of mice after L. m infection (n=10); (D) Bacterial burdens in the organs (brain, lung, spleen, liver).

(E-M) (E) HCAR2$^{+/+}$ and HCAR2$^{-/-}$ mice were treated with ketogenic diet and control diet for 4 weeks separately, and then intraperitoneal infected with 2×10^8 CFU L. m (n=5 for each group). (F) Survival rate of mice after L. m infection (n=10); (G) The percentage of the foamy macrophages before and after infection; (H) The intracellular bacterial burden in the macrophages in peripheral blood; (I) Bacterial burdens in the organs (brain, lung, spleen, liver); Cytokine levels of (J) plasma and (K) brain homogenate; (L-M) Representative H&E staining (L) and the pathology scores (M) of cerebral cortex tissue.

Experiments were performed in triplicate. Data are presented as the mean ± SEM. *p < 0.05.**p < 0.01. Abbreviation: ns, nonsignificant.

Figure 7. Levels of BHB is decreased in bacterial meningitis in humans correlating with disease severity.

(A) Schematic diagram of samples of healthy control (n=60) and bacterial meningitis (n=62). The bacterial meningitis patients were divided into three groups according to the serum BHB level.

(B) Serum BHB level from HC and BM patients.

(C-I) (C)Clinical scores, (D) cell counts and (E) protein in cerebrospinal fluid, (F) white blood cells, (G) procalcitonin, (I) erythrocyte sedimentation rate and (F) C-reactive protein in TBM patients with high, moderate, and low level of BHB.

(J-K) Dynamic change of (J) $CD36^{+}$FMφ and (K)serum BHB in TBM patients after admission.

(L) Heatmap of gene expression involved in lipid metabolism in PBMCs from HC and TBM patients.

Data are presented as the mean ± SEM. *p < 0.05.**p < 0.01. Abbreviation: ns, nonsignificant; BM, bacterial meningitis.

Figure S1. Additional results from Identification of foamy macrophage accumulation during the L. monocytogene neuroinvasion.

(A-B) Mice were intraperitoneally infected with 2×10^{8} CFU L. m. (A) Bacterial

burdens in brains and (B) survival were detected. Data are presented as the mean ± SEM. **p < 0.01.

(C) Heat map of cell clusters identified in 10× scRNA-seq dataset, and top 10 enriched genes for each cluster were highlighted. Normalized z-score is used to illustrate the gene expression.

(D) Proportion of each cluster in Fig 1D according to experimental condition.

(E) Gating strategy for analysis of the foamy macrophage in PBMCs.

(F) Flow cytometry sorting of peripheral blood $CD36^+$ and $CD36^-$ macrophages and sorted cells were stained with BODIPY493/503 and oil Red O. Scale bar, 10 μm.

(G) Mean fluorescence intensity (MFI) of Dil ox-LDL. Data are presented as the mean ± SEM. **p < 0.01.

Figure S2. Additional results from the adoptive transfer of foamy macrophages, Related to Figure 2.

(A) The proportion of $CD36^+$ foamy macrophages under different concentrations of ox-LDL.

(B) The intracellular bacterial burden of the macrophages challenged with L. m (MOI = 10) under different concentrations of ox-LDL.

(C-G) Mice were intraperitoneal infected with 2×10^8 CFU L. m. (C) clinical scores; (D) percentages of weight loss; (E) Bacterial burdens in other tissues (lung, spleen, liver); (F-G) Representative H&E staining (F) and the pathology scores (G) of

cerebral cortex tissue.

(H-I) Bacterial burdens in brains (H) and other tissues (I) from mice after intraperitoneal infection with 5×10^7 CFU L. m.

Experiments were performed in triplicate. Data are presented as the mean ± SEM. *$p < 0.05$.**$p < 0.01$. Abbreviation: ns, nonsignificant.

Figure S3. Accumulation of foamy macrophage exacerbated the intracellular bacteria neuroinvasion.

(A-F) Mice were intraperitoneally infected with 2×10^8 CFU bacteria (S. Typhimurium (A-B), MRSA (C-D) and S. pneumoniae (E-F)). (A, C, E) Flow cytometry analysis of the percentage of the foamy macrophages during the neuroinvasion. (B, D, F) Correlation between the percentage of the foamy macrophages and the bacterial burdens

(G-K) Mice were intraperitoneal infected with 2×10^8 CFU MRSA. (n=5 for each group) (G) Survival rate of mice (n=10); (H) Bacterial burdens in the brain and (I) other tissues; (J-K) Cytokine levels of plasma and brain homogenate.

(L-O) Mice were intraperitoneal infected with 2×10^8 CFU S. pneumoniae. (n=5 for each group) (L) Survival rate of mice (n=10); (M) Bacterial burdens in the tissues; (N-O) Cytokine levels of plasma and brain homogenate.

Data are presented as the mean ± SEM. *$p < 0.05$.**$p < 0.01$. Abbreviation: ns, nonsignificant.

Figure S4. Additional results from the bidirectional transfer of macrophages from PCSK9$^{+/+}$ and PCSK9$^{-/-}$ mice, Related to Figure 2.

(A-B) (A) Flow cytometry analysis of the lipid droplets in peritoneal macrophages of PCSK9$^{+/+}$ and PCSK9$^{-/-}$ mice. (B) MFI were shown in representative histogram.

(C) Flow cytometry of the percentage of the CD36^{+} foamy macrophages during the neurolisteriosis in PCSK9$^{+/+}$ and PCSK9$^{-/-}$ mice separately.

(D) The intracellular bacterial burden of L. monocytogene infected peritoneal macrophages (MOI = 10) from PCSK9$^{+/+}$ and PCSK9$^{-/-}$ mice post infection at 2 or 12 h.

(E-G) Mice in Fig. 2H were intraperitoneal infected with L. monocytogene. (E) Bacterial burdens in other tissues (lung, spleen, liver); Cytokine levels of plasma (F) and brain homogenate (G).

(H-J) Mice in Fig. 2H were orally infected with L. monocytogene. (H) Bacterial burdens in other tissues (lung, spleen, liver); Cytokine levels of plasma (I) and brain homogenate (J).

Experiments were performed in triplicate. Data are presented as the mean ± SEM. *$p < 0.05$.**$p < 0.01$. Abbreviation: ns, nonsignificant.

Figure S5. Additional results from the live-cell flow chamber assays, Related to Figure 3.

(A-B) Optical images of infected macrophages, with or without ox-LDL stimulation adhesion, on the surface of monolayer endothelial cells (A) with different densities

and (C) derived from different tissues (cerebrovascular cells (CVCs), pulmonary vascular endothelial cells (PVECs) and liver sinusoidal endothelial cells (LSECs)). Scale bar, 200 μm. (B, D) Adherent cell count of each group were quantified.

(E) Schematic trajectory used for defining infected macrophage crawling parameters.

(F) Crawling duration of macrophages after securely adhering on the surface of monolayer endothelial cells.

(G) Relative intensity of infected macrophages on epithelial surface were quantified over the time.

Experiments were performed in triplicate. Data are presented as the mean ± SEM. *$p < 0.05$.**$p < 0.01$. Abbreviation: ns, nonsignificant.

Figure S6. Additional results from the influence of β-hydroxybutyrate on the macrophages during the neuroinvasion, Related to Figure 4.

(A) KEGG enrichment analysis of lipid metabolites.

(B) Mass spectrometry analysis of BHB in meningitis mice and control group.

(C-D) mRNA expression of the gene transcripts regulating ketogenesis in the liver (Hmgcs2, Cpt1a).

(E-F) (E)Body weight and (F) food uptake was monitored every 6h during the neuroinvasion.

(G-H) Dynamics of Serum BHB during the neuroinvasion of (G) MRSA and (H) S. typhimurium.

(I-J) $HCAR2^{+/+}$ and $HCAR2^{-/-}$ macrophages was pretreated BHB (10mM) and cAMP

(1mM) for 24h and then infected with L. m (MOI=10). (I) MFI of the BODYPY and (J) intracellular bacterial burden were quantified, respectively.

Experiments were performed in triplicate. Data are presented as the mean ± SEM. *p < 0.05.**p < 0.01. Abbreviation: ns, nonsignificant.

Figure S7. Additional results from the role of β-hydroxybutyrate in regulating the survival of macrophage, Related to Figure 5.

(A-F) Infected macrophages were pretreated with or without BAPTA-AM (10 mM) for 24h.

(A) The intracellular bacterial burden in the upper chamber.

(B-C) (B)Time-lapse confocal images of CHMP4-GFP-expressing of macrophages with BHB (10mM) for 0, 5, 10, 15, 20, 30 min. (C) CHMP4-GFP puncta were quantified.

(D-E) (D) Flow cytometry of LAMP1 expression on the cell surface. (E) MFI was quantified.

(F) Percentage of released enzymes activity in the cell culture medium.

Experiments were performed in triplicate. Data are presented as the mean ± SEM. *p < 0.05.**p < 0.01. Abbreviation: ns, nonsignificant.

Figure S8. Additional results from the effect of ketogenesis in bacterial neuroinvasion, Related to Figure 6.

(A) Clinical scores of mice in Figure 6A.

(B-C) (B) Clinical score and (C) percentages of weight loss in Figure 6D.

(D-G) HCAR2$^{+/+}$ and HCAR2$^{-/-}$ mice were treated with ketogenic diet and control diet for 4 weeks separately, and then orally infected with 2×10^8 CFU L. m (n=5 for each group). (D) Survival rate of mice after L. m infection (n=10); (E) Bacterial burdens in the organs (brain, lung, spleen, liver); Cytokine levels of (F) plasma and (G) brain homogenate.

(H-J) C57BL/6 mice were treated with ketogenic diet and control diet for 4 weeks separately, and then intravenously infected with 2×10^8 CFU MRSA (n=5 for each group). (H) Survival rate of mice after MRSA infection (n=15). (I) Bacterial burdens in the organs (brain, lung, spleen, liver). (J) Clinical scores.

Data are presented as the mean ± SEM. *$p < 0.05$.**$p < 0.01$. Abbreviation: ns, nonsignificant.

Figure S9. Additional results from high levels of BHB and tuberculous meningitis in humans Related to Figure 7.

(A-D) (A) Serum glucose level (C) insulin and from HC and BM patients. (B) Correlation between serum glucose level and BHB in BM patients. (D) Correlation between serum insulin level and BHB in BM patients. R2, spearman correlation coefficient

(E-F) (E)Serum triglyceride (TC), (F) high density lipoprotein (HDC-C) and (G) low density lipoprotein (LDL-C) from HC and TBM patients.

Data are presented as the mean ± SEM. *$p < 0.05$.**$p < 0.01$. Abbreviation: ns,

nonsignificant, HC, health control, BM, bacterial meningitis.

EXPERIMENTAL MODEL AND STUDY PARTICIPANT DETAILS

Clinical samples

Tuberculous meningitis (TBM) disease subjects (n = 62, 32 males and 30 females, aged 41.62 ±15.68 years) and healthy donors (n = 60, 30 males and 30 females, aged 38.32±9.17 years) were recruited from Chongqing Public Health Medical Center. Isolation of PBMCs and single-cell suspensions was performed using PBMC Isolation Kit (P8680, Solarbio) by density gradient centrifugation. Plasma was collected from each patient and donor and then used for quantification of BHB. This study was carried out in strict accordance with the Guidelines for the Care and Use of Animals of Chongqing University, and was compliant with the "Guidance of the Ministry of Science and Technology (MOST) for the Review and Approval of Human Genetic Resources". Healthy individuals and patients providing blood samples were given informed consent. The ethics committee approved this consent procedure. The clinical symptoms of the TBM patients included burnout, headache, irritability, vomiting, fever, neck stiffness, convulsion, and consciousness disorder. Each symptom is worth 1 point.

Animal

All animal experiments were performed following institutional guidelines at Chongqing University. In all experiments, control and experimental mice were 6–8-week-old littermates of male C57BL/6 mice. Littermates of the same sex were housed together regardless of genotype. All mice were maintained under a 12-hour light-dark cycle with ad libitum access to regular food and water.

Bacterial strains

L. monocytogenes (19115) and S. pneumoniae 49619 were grown in Brain Heart Infusion Broth. MRSA USA300 and S. Typhimurium were grown in Luria-Bertani Broth.

METHOD DETAILS

Single cell RNA-sequencing analysis

Isolated PBMCs from the mice were transported in in sterile culture dish with 10 ml Dulbecco's Phosphate-Buffered Saline (DPBS, Thermo Fisher Scientific) on ice to remove the residual tissue storage solution, then minced on ice. We used dissociation enzyme 0.25% Trypsin (Thermo Fisher Scientific) and 10 ug/mL DNase I (Sigma) dissolved in PBS with 5% Fetal Bovine Serum (FBS, GIBCO) to digest the tissues. PBMCs were dissociated at 37 ℃ with a shaking speed of 50 rpm for about 40 min. We repeatedly collected the dissociated cells at interval of 20 min to increase cell yield and viability. Cell suspensions were filtered using a 40 μm nylon cell strainer and red blood cells were removed by red blood cell lysis solution (Thermo Fisher Scientific). Dissociated cells were washed with DPBS containing 2% FBS.

10× beads were then subject to second-strand cDNA synthesis, adaptor ligation, and universal amplification. Sequencing libraries were prepared using randomly interrupted whole-transcriptome amplification products to enrich the 3’ end of the transcripts linked with the cell barcode and UMI. All the remaining procedures including the library construction were performed according to the standard

manufacturer's protocol (Chromium Single Cell 3' v3). Sequencing libraries were quantified using a High Sensitivity DNA Chip (Agilent) on a Bioanalyzer 2100 and the Qubit High Sensitivity DNA Assay (Thermo Fisher Scientific). The libraries were sequenced on NovaSeq6000 (Illumina) using 2x150 chemistry. The sequencing and bioinformatic analysis were performed on platform of Majorbio Co., Ltd (Shanghai, China).

Reads were processed using the Cell Ranger (v7.1.0) pipeline with default and recommended parameters. FASTQs generated from Illumina sequencing output were aligned to the mouse genome, version GRCm38, using the STAR algorithm. Gene-barcode matrix containing the barcoded cells and gene expression counts were generated. This output was then imported into the Seurat (v3.2.0) R toolkit for quality control and downstream analysis of our single cell RNAseq data.

Cells were clustered using graph-based clustering of the PCA reduced data with the Louvain Method after computing a shared nearest neighbor graph. For sub-clustering, we applied the same procedure of scaled, dimensionality reduction, and clustering to the specific set of data. For each cluster, we used the Wilcoxon Rank-Sum Test to find significant deferentially expressed genes comparing to the remaining clusters.

Mouse model of acute bacteria brain neuroinvasion

Mice were infected with 2×10^8 CFU bacteria and weighed and scored every 3 h. The progression of acute bacterial meningitis was determined as previously described with a few adaptations[68]. Scoring was performed based on the Table S1, including activity (0–2), time to return to upright position (0–2), eyes (0–2) and neurological

examination (0–2). Mice were deeply anaesthetized by an intraperitoneal injection of tribromoethanol solution (Avertin, 500 mg/kg) and transcranial perfused with saline solution. Blood was sampled immediately before perfusion. Tissue samples, including brain, lung, liver, and spleen, were dissected and weighed.

Analysis Bacterial load in cell or tissue

After 24 h infection, tissues were transferred into 2 ml tubes containing 4 mm stainless steel beads (Qiagen) and 1 ml of ice-cold sterile saline. Samples were homogenized in TissueLyser II (Qiagen) for 5 min at 70 Hz. Serial dilutions of the homogenates were plated on the plates incubated at 37℃ and CFU were counted. The infected macrophages were further incubated in a fresh solution containing 5 μg/mL lysostaphin for the indicated periods. Cells were lysed to release intracellular bacteria and diluted to appropriate dilutions with sterile PBS for CFU count on agar plates.

Brain histopathology and Immunostaining

Brain samples were collected from infected mice 24 h after injection. Mice were deeply anaesthetized with tribromoethanol solution (Avertin, 500 mg/kg, intravenously) and transcranial perfused with 30 ml saline solution followed by 10 ml of 4% PFA in saline. After dissection, brain samples were maintained in 4% PFA at 4 ℃. Fixed brains were embedded in paraffin, sectioned and half of the slides were stained using haematoxylin and eosin. Each field was assigned a score from 0 to 3 based on neuronal morphology: grade 0 (not altered); grade 1 (no vacuolation with small numbers of pyknotic cells); grade 2 (moderate vacuolation and pyknosis); and

grade 3 (extensive vacuolation, pyknosis and tissue loss or liquefactive necrosis). Fresh frozen brain tissue sections of 5-10 mm thickness were mounted on slides, air dried for 10 minutes at room temperature and fixed in ice cold 10% neutral-buffered formalin for 5-10 minutes. Slices were washed in PBS, then incubated for 2 h in 3% bovine serum albumin (BSA) and then 0.1% Triton X-100 in PBS. and were labelled with the appropriate primary antibodies of CD11b overnight at 4 °C in mild blocking conditions. Next day, the slices were washed in PBS, and then incubated with secondary antibodies, BODIPY FL (MedChemExpress) and DAPI. Tissues were washed in PBS and then mounted on glass slides under coverslips in mounting medium. The slides were left in darkness overnight before observation under a Zeiss LSM900 or LM710 microscope.

Cell sorting and flow cytometry.

Isolated mouse PBMCs were cleaned twice with PBS. After calculating and determining the appropriate concentration, appropriate amount of fluorescent-coupled primary antibody (F4/80-PE, CD11b-FITC, as the marker of macrophage, CD36-APC) was added respectively. Incubate at 4 °C for 30 minutes away from light. The living macrophages were collected according to the expression of CD36 and then culture in vitro overnight. The sorting cells were detected the lipid content using BODIPY FL and oil Red O. To evaluate the ability of lipid uptake, macrophages were incubated with 40 μg/ml DiI-ox-LDL particles for 6h and then detect the fluorescence intensity by flow cytometry.

To determine the proportion of foamy macrophages population, cells were stained

with fluorescent-coupled primary antibody (F4/80-PE, CD11b-FITC) at 4 °C for 30 minutes and then BODYPY at room temperature and away from light for 15 minutes. To detect the expression of LAMP1 on the cell surface, infected macrophages were cleaned twice with PBS and then stained with LAMP1-FITC at 4 °C for 30 minutes away from light. The cells were washed three times and then re-suspended in 200μl of the staining buffer for final FACS analysis. Data was analyzed with FlowJo software.

Isolation and culture of primary cells

To generate peritoneal macrophages, 8-week-old mice were injected i.p. with 3% thioglycolate broth. After 72 h, peritoneal cells were harvested, and macrophages were enriched by quick adherence.

Primary endothelial cells were isolated from 8 to 12-week-old male C57BL/6 mice. The cerebral cortex in the brains were separated and rolled on the filter paper to remove the meninges and choroid plexuses. A mechanical reduction was performed by mincing the brain pieces using surgical blades. The homogenate was centrifuged (800 g, 8 min, 4°C) and the precipitate was digested in DMEM containing 1 mg/mL type II collagenase and 58.5 U/mL type I DNase for 75 min on a benchtop orbital shaker at 37°C. The supernatant was finally collected and centrifuged at 500×g for 8 min. The isolated cerebrovascular endothelial cells were purified by the anchoring technique. The liver and lung from an anaesthetized mouse were perfused via the portal vein sequentially with balanced salt solution containing 5 mM glucose, 0.01% sodium heparin, and 5 mM EGTA and high glucose DMEM medium containing 4 mM $CaCl_2$, 2% FBS and 0.05% collagenase IV (Sigma-Aldrich, St. Louis, MO) at a

flow rate of 5 ml/min for 5 min, respectively. The following steps are similar in order to separate the liver sinusoids endothelial cells and pulmonary vascular endothelial cells.

Isolation of primary embryonic neurons and single-cell suspensions was performed using Pierce Primary Neuron Isolation Kit (88280, Thermo Scientific) by density gradient centrifugation.

In vitro blood-brain barrier

The in vitro BBB model was constructed with primary endothelial cells using a transwell cell culture system. Briefly, brain microvascular endothelial cells (1×10^5 cells/well) were seeded onto the upper chamber of the transwell pre-coated with gelatine in 24-well plates, and cultured with the medium containing 10% FBS. The integrity of the cell monolayer was evaluated by measuring the TEER values using a Millicell-ERS voltohmmeter (Millipore). The cell monolayers with TEER values higher than 300 $\Omega.cm^2$ were used as the BBB model for the transmigration studies. The neurons cells were seeded onto the lower chamber of the transwell for bacterial load.

Macrophages were stimulated with different concentration of ox-LDL and then challenged with L. monocytogenes (MOI = 10) for 2 h. After the BBB model has been constructed, the infected macrophages were digested for cell counting (5×10^4 cells/well) and added into the upper chamber. The conventional incubation time was 12h and then the neurons cells in the bottom chamber were lysed for penetrating bacterial quantification.

Foamy Macrophages transmission in mouse bacteria brain neuroinvasion

Peritoneal macrophages of the donor mice were obtained by intraperitoneal injection of thioglycolate and after further culture, we got the purified macrophages. Foamy macrophages were collected by stimulating purified macrophages with ox-LDL for 24h. The recipient mice were pretreated with intraperitoneal injection of CTX for 3 days and then given 0.2 ml normal saline or cell suspension (1×10^6 per mouse) by intraperitoneal injection at Day 0. Recipient mice were infected 12 h post-transplantation and euthanized after 18h.

Purified peritoneal macrophages were obtained from $PCSK9^{+/+}$ and $PCSK9^{-/-}$ donor mice respectively, and then transferred to recipient mice as shown in Fig.2H. Recipient mice were infected with with 2×10^8 CFU L. monocytogene 12 h post-transplantation and euthanized after 24 h.

Live-cell flow chamber assay

A flow cell system was used to test macrophages adhesion, shear resistance, crawling, and transmigration, on endotheliocytes. Shear flow was applied by a syringe pump. Different shear stresses were acquired by setting corresponding volumetric flow rates. Isolated macrophages were stimulated under different concentration of ox-LDL for 24 h and then infected with L. monocytogene (MOI=5). Macrophages were re-suspended and stained with Hoechst. The cells were then perfused over pre-formed endotheliocytes monolayer for 8 min at a shear stress of 0.1 dyne/cm^2. Then, the adhesion and crawling dynamics of macrophages on endotheliocytes monolayer was recorded at 2 dyne/cm^2 for 2 min at 20× objective by a CCD camera. Images were

taken from the video every second and analyzed the crawling parameters and transmigrating duration with Image J software. Here a transmigrated macrophage was determined by 70% decrease of fluorescence intensity when it is transmigrating cross the monolayer.

For testing shear-resistant macrophage adhesion, preprocessed macrophages were re-suspended and counted. The same number of cells (2×10^4) were completely perfused over pre-formed endotheliocytes monolayer. The shear stress was increased stepwise from 1 to 2, 4, 8, 16, 32 dyne/cm^2 for 30s each. Remaining adherent macrophages on endotheliocytes monolayer were recorded at 20× objective by a CCD camera and counted using Image J software. The normalized adhesion fraction was calculated by dividing the number of adherent macrophages at the endpoint of each shear phase by the number at the endpoint of 1 dyne/cm^2. For defining the macrophage transmigration dynamics, the time-lapse images were analyzed offline frame-by-frame every second.

Quantification of L. monocytogene protrusion formation

Isolated peritoneal macrophages were stimulated under different concentration of ox-LDL for 24 h and then infected with CFSE-labeled L. monocytogene (MOI=10). At 4 h post-infection, cells were fixed, permeabilized, and labeled with mouse anti-ezrin and phalloidin-Alexa 647. Samples were analyzed using confocal microscopy. Protrusions were identified as bacteria with ezrin tails that project from host cells into neighboring. In each experiment, ten cells were scored for each condition. The lengths of ezrin comet tails were measured using ImageJ software

Lipid metabolomics

Metabolite extraction and mass spectrometry detection was processed using Ultra-High Performance Liquid Chromatography-mass spectrometry (UHPLC-MS) of Biomarker Technologies (Beijing, China). The raw data collected using MassLynx V4.2 is processed by Progenesis QI software for peak extraction, peak alignment, and other data processing operations, based on the Progenesis QI software online METLIN database and Biomark's self-built library for identification. The theoretical fragment identification and mass deviation are within 100ppm. After normalizing the original peak area information with the total peak area, the follow-up analysis was performed. Principal component analysis (PCA) and Spearman correlation analysis were used to judge the repeatability of the samples within group and the quantity control samples. The identified compounds are searched for classification and pathway information in KEGG and HMDB databases.

A total of 4,625 named metabolites were retained for datasets. The R language package ropls was used to perform OPLS-DA modeling, and 200 times permutation tests was performed to verify the reliability of the model. The screening criteria are FC>1, P value<0.05 and VIP>1. The difference metabolites of KEGG pathway enrichment significance were calculated using hypergeometric distribution test.

Fura-4 Ca2 + imaging

Cells were removed from incubator and washed with PBS and then incubated with 5 μM Fluo-4 AM (Beyotime) for 60 min at 37 °C with 0.04% Pluronic-127. After incubation, cells were washed with PBS and incubated with PBS for 30 min at 37 °C.

Fluorescence were detected with a CytoFLEX Flow Cytometer (Beckman Coulter) equipped with 488 nm excitation wavelength. As indicated, BHB (10 mM) were added into the cells pre-loaded with Fluo4 30s after the record. Data was analyzed with Flow Jo to determine the fluorescence intensity.

Diet studies

Mice were supplemented with 20 mg/ml ketone ester (D-β-hydroxybutyrate-(R)-1,3 butanediol monoester) in the drinking water for 4 weeks before the infection. Control diet (23.2% protein, 2.8% fat and 74% sugar) and ketogenic diet (10% protein, 90% fat) were purchased from Xietong Pharma Co. Mice were placed on ketogenic or control diets for 4 weeks before the infection.

RT–qPCR

Total RNA was isolated using a RNeasy Mini Kit (QIAGEN). The mRNA was reverse-transcribed and quantified using an HiScript II 1st Strand cDNA Synthesis Kit (Vazyme). qRT-PCR was performed on an ABI StepOnePlus PCR system (Thermo Fisher Scientific), and results were normalized to GAPDH mRNA levels. Data were analyzed using the 2-DDct method. The Primer sequences were provided in Table 4.

QUANTIFICATION AND STATISTICAL ANALYSIS

Statistical analysis was performed using GraphPad Prism and OriginPro Software. Two-group comparisons were made using two-tailed unpaired Student's t-test. One-way analysis of variance (ANOVA) with appropriate multiple comparisons tests was used to compare three independent groups. For comparisons of multiple factors, two-

way ANOVA with appropriate multiple comparisons tests was used. Exact *p* values for specific group comparisons in all the figures. A value of $p < 0.05$ was considered significant. Specific details of statistical analysis are presented above or in associated figure legends.

To identify DEGs (differential expression genes) between two different samples or clusters, was performed using the function FindMarkers in Seurat, using a likelihood ratio test. Essentially, DEGs with $|\log2FC| > 0.25$ and Q value ≤ 0.05 were significantly different expressed genes. In addition, functional-enrichment analysis GO were performed to identify which DEGs were significantly enriched in GO terms and metabolic pathways at Bonferroni-corrected P-value ≤ 0.05 compared with the whole-transcriptome background. GO functional enrichment analysis were carried out by Goatools (https://github.com/tanghaibao/Goatools).

Reference

1. Doran, K.S., Fulde, M., Gratz, N., Kim, B.J., Nau, R., Prasadarao, N., Schubert-Unkmeir, A., Tuomanen, E.I., and Valentin-Weigand, P. (2016). Host-pathogen interactions in bacterial meningitis. Acta Neuropathol *131*, 185-209. 10.1007/s00401-015-1531-z.
2. Hasbun, R. (2022). Progress and Challenges in Bacterial Meningitis: A Review. JAMA *328*, 2147-2154. 10.1001/jama.2022.20521.
3. Rua, R., and McGavern, D.B. (2018). Advances in Meningeal Immunity. Trends Mol Med *24*, 542-559. 10.1016/j.molmed.2018.04.003.

4. Merlini, A., Haberl, M., Strauss, J., Hildebrand, L., Genc, N., Franz, J., Chilov, D., Alitalo, K., Flugel-Koch, C., Stadelmann, C., et al. (2022). Distinct roles of the meningeal layers in CNS autoimmunity. Nat Neurosci *25*, 887-899. 10.1038/s41593-022-01108-3.

5. Byrd, T.F., and Davis, L.E. (2007). Multidrug-resistant tuberculous meningitis. Curr Neurol Neurosci Rep *7*, 470-475. 10.1007/s11910-007-0073-8.

6. Huynh, J., Donovan, J., Phu, N.H., Nghia, H.D.T., Thuong, N.T.T., and Thwaites, G.E. (2022). Tuberculous meningitis: progress and remaining questions. Lancet Neurol *21*, 450-464. 10.1016/S1474-4422(21)00435-X.

7. van de Beek, D., Brouwer, M.C., Koedel, U., and Wall, E.C. (2021). Community-acquired bacterial meningitis. Lancet *398*, 1171-1183. 10.1016/S0140-6736(21)00883-7.

8. Levin, B.R., Baquero, F., Ankomah, P.P., and McCall, I.C. (2017). Phagocytes, Antibiotics, and Self-Limiting Bacterial Infections. Trends Microbiol *25*, 878-892. 10.1016/j.tim.2017.07.005.

9. Boada-Romero, E., Martinez, J., Heckmann, B.L., and Green, D.R. (2020). The clearance of dead cells by efferocytosis. Nat Rev Mol Cell Biol *21*, 398-414. 10.1038/s41580-020-0232-1.

10. Locati, M., Curtale, G., and Mantovani, A. (2020). Diversity, Mechanisms, and Significance of Macrophage Plasticity. Annu Rev Pathol *15*, 123-147. 10.1146/annurev-pathmechdis-012418-012718.

11. Zhai, L., Huang, C., Ning, Z., Zhang, Y., Zhuang, M., Yang, W., Wang, X.,

Wang, J., Zhang, L., Xiao, H., et al. (2023). Ruminococcus gnavus plays a pathogenic role in diarrhea-predominant irritable bowel syndrome by increasing serotonin biosynthesis. Cell Host Microbe *31*, 33-44 e35. 10.1016/j.chom.2022.11.006.

12. Van der Merwe, S., Chokshi, S., Bernsmeier, C., and Albillos, A. (2021). The multifactorial mechanisms of bacterial infection in decompensated cirrhosis. J Hepatol *75 Suppl 1*, S82-S100. 10.1016/j.jhep.2020.11.029.

13. Surewaard, B.G.J., Thanabalasuriar, A., Zeng, Z., Tkaczyk, C., Cohen, T.S., Bardoel, B.W., Jorch, S.K., Deppermann, C., Bubeck Wardenburg, J., Davis, R.P., et al. (2018). alpha-Toxin Induces Platelet Aggregation and Liver Injury during Staphylococcus aureus Sepsis. Cell Host Microbe *24*, 271-284 e273. 10.1016/j.chom.2018.06.017.

14. Aegerter, H., Lambrecht, B.N., and Jakubzick, C.V. (2022). Biology of lung macrophages in health and disease. Immunity *55*, 1564-1580. 10.1016/j.immuni.2022.08.010.

15. Maudet, C., Kheloufi, M., Levallois, S., Gaillard, J., Huang, L., Gaultier, C., Tsai, Y.H., Disson, O., and Lecuit, M. (2022). Bacterial inhibition of Fas-mediated killing promotes neuroinvasion and persistence. Nature *603*, 900-906. 10.1038/s41586-022-04505-7.

16. Xu, K., Yin, N., Peng, M., Stamatiades, E.G., Shyu, A., Li, P., Zhang, X., Do, M.H., Wang, Z., Capistrano, K.J., et al. (2021). Glycolysis fuels phosphoinositide 3-kinase signaling to bolster T cell immunity. Science *371*,

405-410. 10.1126/science.abb2683.

17. Escoll, P., Song, O.R., Viana, F., Steiner, B., Lagache, T., Olivo-Marin, J.C., Impens, F., Brodin, P., Hilbi, H., and Buchrieser, C. (2017). Legionella pneumophila Modulates Mitochondrial Dynamics to Trigger Metabolic Repurposing of Infected Macrophages. Cell Host Microbe *22*, 302-316 e307. 10.1016/j.chom.2017.07.020.

18. Yang, D., Jacobson, A., Meerschaert, K.A., Sifakis, J.J., Wu, M., Chen, X., Yang, T., Zhou, Y., Anekal, P.V., Rucker, R.A., et al. (2022). Nociceptor neurons direct goblet cells via a CGRP-RAMP1 axis to drive mucus production and gut barrier protection. Cell *185*, 4190-4205 e4125. 10.1016/j.cell.2022.09.024.

19. Loft, A., Schmidt, S.F., Caratti, G., Stifel, U., Havelund, J., Sekar, R., Kwon, Y., Sulaj, A., Chow, K.K., Alfaro, A.J., et al. (2022). A macrophage-hepatocyte glucocorticoid receptor axis coordinates fasting ketogenesis. Cell Metab *34*, 473-486 e479. 10.1016/j.cmet.2022.01.004.

20. Puchalska, P., and Crawford, P.A. (2017). Multi-dimensional Roles of Ketone Bodies in Fuel Metabolism, Signaling, and Therapeutics. Cell Metab *25*, 262-284. 10.1016/j.cmet.2016.12.022.

21. Tomlinson, K.L., Chen, Y.T., Junker, A., Urso, A., Wong Fok Lung, T., Ahn, D., Hofstaedter, C.E., Baskota, S.U., Ernst, R.K., Prince, A., and Riquelme, S.A. (2023). Ketogenesis promotes tolerance to Pseudomonas aeruginosa pulmonary infection. Cell Metab *35*, 1767-1781 e1766.

10.1016/j.cmet.2023.09.001.

22. Goldberg, E.L., Molony, R.D., Kudo, E., Sidorov, S., Kong, Y., Dixit, V.D., and Iwasaki, A. (2019). Ketogenic diet activates protective gammadelta T cell responses against influenza virus infection. Sci Immunol *4*. 10.1126/sciimmunol.aav2026.

23. Seufert, A.L., Hickman, J.W., Traxler, S.K., Peterson, R.M., Waugh, T.A., Lashley, S.J., Shulzhenko, N., Napier, R.J., and Napier, B.A. (2022). Enriched dietary saturated fatty acids induce trained immunity via ceramide production that enhances severity of endotoxemia and clearance of infection. Elife *11*. 10.7554/eLife.76744.

24. Wilhelm, C., Surendar, J., and Karagiannis, F. (2021). Enemy or ally? Fasting as an essential regulator of immune responses. Trends Immunol *42*, 389-400. 10.1016/j.it.2021.03.007.

25. Singh, V., Jamwal, S., Jain, R., Verma, P., Gokhale, R., and Rao, K.V. (2012). Mycobacterium tuberculosis-driven targeted recalibration of macrophage lipid homeostasis promotes the foamy phenotype. Cell Host Microbe *12*, 669-681. 10.1016/j.chom.2012.09.012.

26. McFarland, A.P., Yalin, A., Wang, S.Y., Cortez, V.S., Landsberger, T., Sudan, R., Peng, V., Miller, H.L., Ricci, B., David, E., et al. (2021). Multi-tissue single-cell analysis deconstructs the complex programs of mouse natural killer and type 1 innate lymphoid cells in tissues and circulation. Immunity *54*, 1320-1337 e1324. 10.1016/j.immuni.2021.03.024.

27. Ahmad, F., Rani, A., Alam, A., Zarin, S., Pandey, S., Singh, H., Hasnain, S.E., and Ehtesham, N.Z. (2022). Macrophage: A Cell With Many Faces and Functions in Tuberculosis. Front Immunol *13*, 747799. 10.3389/fimmu.2022.747799.

28. Flannagan, R.S., and Heinrichs, D.E. (2020). Macrophage-driven nutrient delivery to phagosomal Staphylococcus aureus supports bacterial growth. EMBO Rep *21*, e50348. 10.15252/embr.202050348.

29. Hill, D.A., Lim, H.W., Kim, Y.H., Ho, W.Y., Foong, Y.H., Nelson, V.L., Nguyen, H.C.B., Chegireddy, K., Kim, J., Habertheuer, A., et al. (2018). Distinct macrophage populations direct inflammatory versus physiological changes in adipose tissue. Proc Natl Acad Sci U S A *115*, E5096-E5105. 10.1073/pnas.1802611115.

30. Jaitin, D.A., Adlung, L., Thaiss, C.A., Weiner, A., Li, B., Descamps, H., Lundgren, P., Bleriot, C., Liu, Z., Deczkowska, A., et al. (2019). Lipid-Associated Macrophages Control Metabolic Homeostasis in a Trem2-Dependent Manner. Cell *178*, 686-698 e614. 10.1016/j.cell.2019.05.054.

31. Luis, G., Godfroid, A., Nishiumi, S., Cimino, J., Blacher, S., Maquoi, E., Wery, C., Collignon, A., Longuespee, R., Montero-Ruiz, L., et al. (2021). Tumor resistance to ferroptosis driven by Stearoyl-CoA Desaturase-1 (SCD1) in cancer cells and Fatty Acid Biding Protein-4 (FABP4) in tumor microenvironment promote tumor recurrence. Redox Biol *43*, 102006. 10.1016/j.redox.2021.102006.

32. Victor, M.B., Leary, N., Luna, X., Meharena, H.S., Scannail, A.N., Bozzelli, P.L., Samaan, G., Murdock, M.H., von Maydell, D., Effenberger, A.H., et al. (2022). Lipid accumulation induced by APOE4 impairs microglial surveillance of neuronal-network activity. Cell Stem Cell *29*, 1197-1212 e1198. 10.1016/j.stem.2022.07.005.

33. Xu, S., Chaudhary, O., Rodriguez-Morales, P., Sun, X., Chen, D., Zappasodi, R., Xu, Z., Pinto, A.F.M., Williams, A., Schulze, I., et al. (2021). Uptake of oxidized lipids by the scavenger receptor CD36 promotes lipid peroxidation and dysfunction in CD8(+) T cells in tumors. Immunity *54*, 1561-1577 e1567. 10.1016/j.immuni.2021.05.003.

34. Guerrini, V., and Gennaro, M.L. (2019). Foam Cells: One Size Doesn't Fit All. Trends Immunol *40*, 1163-1179. 10.1016/j.it.2019.10.002.

35. Luo, Y., Duan, H., Qian, Y., Feng, L., Wu, Z., Wang, F., Feng, J., Yang, D., Qin, Z., and Yan, X. (2017). Macrophagic CD146 promotes foam cell formation and retention during atherosclerosis. Cell Res *27*, 352-372. 10.1038/cr.2017.8.

36. Kim, K., Shim, D., Lee, J.S., Zaitsev, K., Williams, J.W., Kim, K.W., Jang, M.Y., Seok Jang, H., Yun, T.J., Lee, S.H., et al. (2018). Transcriptome Analysis Reveals Nonfoamy Rather Than Foamy Plaque Macrophages Are Proinflammatory in Atherosclerotic Murine Models. Circ Res *123*, 1127-1142. 10.1161/CIRCRESAHA.118.312804.

37. Botham, K.M., and Wheeler-Jones, C.P. (2013). Postprandial lipoproteins and the molecular regulation of vascular homeostasis. Prog Lipid Res *52*, 446-464.

10.1016/j.plipres.2013.06.001.

38. Jaggi, U., Matundan, H.H., Yu, J., Hirose, S., Mueller, M., Wormley, F.L., Jr., and Ghiasi, H. (2021). Essential role of M1 macrophages in blocking cytokine storm and pathology associated with murine HSV-1 infection. PLoS Pathog *17*, e1009999. 10.1371/journal.ppat.1009999.

39. Pasula, R., Martin, W.J., 2nd, Kesavalu, B.R., Abdalla, M.Y., and Britigan, B.E. (2017). Passive transfer of interferon-gamma over-expressing macrophages enhances resistance of SCID mice to Mycobacterium tuberculosis infection. Cytokine *95*, 70-79. 10.1016/j.cyto.2017.02.009.

40. Russell, D.G., Cardona, P.J., Kim, M.J., Allain, S., and Altare, F. (2009). Foamy macrophages and the progression of the human tuberculosis granuloma. Nat Immunol *10*, 943-948. 10.1038/ni.1781.

41. Peyrusson, F., Varet, H., Nguyen, T.K., Legendre, R., Sismeiro, O., Coppee, J.Y., Wolz, C., Tenson, T., and Van Bambeke, F. (2020). Intracellular Staphylococcus aureus persisters upon antibiotic exposure. Nat Commun *11*, 2200. 10.1038/s41467-020-15966-7.

42. Ding, Z., Pothineni, N.V.K., Goel, A., Luscher, T.F., and Mehta, J.L. (2020). PCSK9 and inflammation: role of shear stress, pro-inflammatory cytokines, and LOX-1. Cardiovasc Res *116*, 908-915. 10.1093/cvr/cvz313.

43. Da Dalt, L., Castiglioni, L., Baragetti, A., Audano, M., Svecla, M., Bonacina, F., Pedretti, S., Uboldi, P., Benzoni, P., Giannetti, F., et al. (2021). PCSK9 deficiency rewires heart metabolism and drives heart failure with preserved

ejection fraction. Eur Heart J *42*, 3078-3090. 10.1093/eurheartj/ehab431.

44. Katsuki, S., P, K.J., Lupieri, A., Nakano, T., Passos, L.S.A., Rogers, M.A., Becker-Greene, D., Le, T.D., Decano, J.L., Ho Lee, L., et al. (2022). Proprotein Convertase Subtilisin/Kexin 9 (PCSK9) Promotes Macrophage Activation via LDL Receptor-Independent Mechanisms. Circ Res *131*, 873-889. 10.1161/CIRCRESAHA.121.320056.

45. Qi, Z., Hu, L., Zhang, J., Yang, W., Liu, X., Jia, D., Yao, Z., Chang, L., Pan, G., Zhong, H., et al. (2021). PCSK9 (Proprotein Convertase Subtilisin/Kexin 9) Enhances Platelet Activation, Thrombosis, and Myocardial Infarct Expansion by Binding to Platelet CD36. Circulation *143*, 45-61. 10.1161/CIRCULATIONAHA.120.046290.

46. Neupane, A.S., Willson, M., Chojnacki, A.K., Vargas, E.S.C.F., Morehouse, C., Carestia, A., Keller, A.E., Peiseler, M., DiGiandomenico, A., Kelly, M.M., et al. (2020). Patrolling Alveolar Macrophages Conceal Bacteria from the Immune System to Maintain Homeostasis. Cell *183*, 110-125 e111. 10.1016/j.cell.2020.08.020.

47. Hernandez, G.E., and Iruela-Arispe, M.L. (2020). The many flavors of monocyte/macrophage--endothelial cell interactions. Curr Opin Hematol *27*, 181-189. 10.1097/MOH.0000000000000573.

48. Pang, X., He, X., Qiu, Z., Zhang, H., Xie, R., Liu, Z., Gu, Y., Zhao, N., Xiang, Q., and Cui, Y. (2023). Targeting integrin pathways: mechanisms and advances in therapy. Signal Transduct Target Ther *8*, 1. 10.1038/s41392-022-01259-6.

49. Deng, L., Kersten, S., and Stienstra, R. (2023). Triacylglycerol uptake and handling by macrophages: From fatty acids to lipoproteins. Prog Lipid Res *92*, 101250. 10.1016/j.plipres.2023.101250.

50. Patterson, M.T., Firulyova, M.M., Xu, Y., Hillman, H., Bishop, C., Zhu, A., Hickok, G.H., Schrank, P.R., Ronayne, C.E., Caillot, Z., et al. (2023). Trem2 promotes foamy macrophage lipid uptake and survival in atherosclerosis. Nature Cardiovascular Research *2*, 1015-1031. 10.1038/s44161-023-00354-3.

51. Andrews, N.W., and Corrotte, M. (2018). Plasma membrane repair. Curr Biol *28*, R392-R397. 10.1016/j.cub.2017.12.034.

52. Jimenez, A.J., Maiuri, P., Lafaurie-Janvore, J., Divoux, S., Piel, M., and Perez, F. (2014). ESCRT machinery is required for plasma membrane repair. Science *343*, 1247136. 10.1126/science.1247136.

53. Newman, J.C., and Verdin, E. (2017). beta-Hydroxybutyrate: A Signaling Metabolite. Annu Rev Nutr *37*, 51-76. 10.1146/annurev-nutr-071816-064916.

54. Youm, Y.H., Nguyen, K.Y., Grant, R.W., Goldberg, E.L., Bodogai, M., Kim, D., D'Agostino, D., Planavsky, N., Lupfer, C., Kanneganti, T.D., et al. (2015). The ketone metabolite beta-hydroxybutyrate blocks NLRP3 inflammasome-mediated inflammatory disease. Nat Med *21*, 263-269. 10.1038/nm.3804.

55. Duking, T., Spieth, L., Berghoff, S.A., Piepkorn, L., Schmidke, A.M., Mitkovski, M., Kannaiyan, N., Hosang, L., Scholz, P., Shaib, A.H., et al. (2022). Ketogenic diet uncovers differential metabolic plasticity of brain cells. Sci Adv *8*, eabo7639. 10.1126/sciadv.abo7639.

56. Lu, J.F., Zhu, M.Q., Xia, B., Zhang, N.N., Liu, X.P., Liu, H., Zhang, R.X., Xiao, J.Y., Yang, H., Zhang, Y.Q., et al. (2023). GDF15 is a major determinant of ketogenic diet-induced weight loss. Cell Metab *35*, 2165-2182 e2167. 10.1016/j.cmet.2023.11.003.

57. Matsuura, T.R., Puchalska, P., Crawford, P.A., and Kelly, D.P. (2023). Ketones and the Heart: Metabolic Principles and Therapeutic Implications. Circ Res *132*, 882-898. 10.1161/CIRCRESAHA.123.321872.

58. Shah, U.A., and Iyengar, N.M. (2022). Plant-Based and Ketogenic Diets As Diverging Paths to Address Cancer: A Review. JAMA Oncol *8*, 1201-1208. 10.1001/jamaoncol.2022.1769.

59. Liu, Y., Li, J.Y., Chen, S.T., Huang, H.R., and Cai, H. (2016). The rLrp of Mycobacterium tuberculosis inhibits proinflammatory cytokine production and downregulates APC function in mouse macrophages via a TLR2-mediated PI3K/Akt pathway activation-dependent mechanism. Cell Mol Immunol *13*, 729-746. 10.1038/cmi.2015.58.

60. Steeb, B., Claudi, B., Burton, N.A., Tienz, P., Schmidt, A., Farhan, H., Maze, A., and Bumann, D. (2013). Parallel exploitation of diverse host nutrients enhances Salmonella virulence. PLoS Pathog *9*, e1003301. 10.1371/journal.ppat.1003301.

61. Jiang, L., Wang, P., Song, X., Zhang, H., Ma, S., Wang, J., Li, W., Lv, R., Liu, X., Ma, S., et al. (2021). Salmonella Typhimurium reprograms macrophage metabolism via T3SS effector SopE2 to promote intracellular replication and

virulence. Nat Commun *12*, 879. 10.1038/s41467-021-21186-4.

62. Allahverdian, S., Chaabane, C., Boukais, K., Francis, G.A., and Bochaton-Piallat, M.L. (2018). Smooth muscle cell fate and plasticity in atherosclerosis. Cardiovasc Res *114*, 540-550. 10.1093/cvr/cvy022.

63. Robichaud, S., Rasheed, A., Pietrangelo, A., Doyoung Kim, A., Boucher, D.M., Emerton, C., Vijithakumar, V., Gharibeh, L., Fairman, G., Mak, E., et al. (2022). Autophagy Is Differentially Regulated in Leukocyte and Nonleukocyte Foam Cells During Atherosclerosis. Circ Res *130*, 831-847. 10.1161/CIRCRESAHA.121.320047.

64. Boven, L.A., Van Meurs, M., Van Zwam, M., Wierenga-Wolf, A., Hintzen, R.Q., Boot, R.G., Aerts, J.M., Amor, S., Nieuwenhuis, E.E., and Laman, J.D. (2006). Myelin-laden macrophages are anti-inflammatory, consistent with foam cells in multiple sclerosis. Brain *129*, 517-526. 10.1093/brain/awh707.

65. Peyron, P., Vaubourgeix, J., Poquet, Y., Levillain, F., Botanch, C., Bardou, F., Daffe, M., Emile, J.F., Marchou, B., Cardona, P.J., et al. (2008). Foamy macrophages from tuberculous patients' granulomas constitute a nutrient-rich reservoir for M. tuberculosis persistence. PLoS Pathog *4*, e1000204. 10.1371/journal.ppat.1000204.

66. Weis, E.M., Puchalska, P., Nelson, A.B., Taylor, J., Moll, I., Hasan, S.S., Dewenter, M., Hagenmuller, M., Fleming, T., Poschet, G., et al. (2022). Ketone body oxidation increases cardiac endothelial cell proliferation. EMBO Mol Med *14*, e14753. 10.15252/emmm.202114753.

67. Karagiannis, F., Peukert, K., Surace, L., Michla, M., Nikolka, F., Fox, M., Weiss, P., Feuerborn, C., Maier, P., Schulz, S., et al. (2022). Impaired ketogenesis ties metabolism to T cell dysfunction in COVID-19. Nature *609*, 801-807. 10.1038/s41586-022-05128-8.

68. Koopmans, M.M., Engelen-Lee, J., Brouwer, M.C., Jaspers, V., Man, W.K., Vall Seron, M., and van de Beek, D. (2018). Characterization of a Listeria monocytogenes meningitis mouse model. J Neuroinflammation *15*, 257. 10.1186/s12974-018-1293-3.

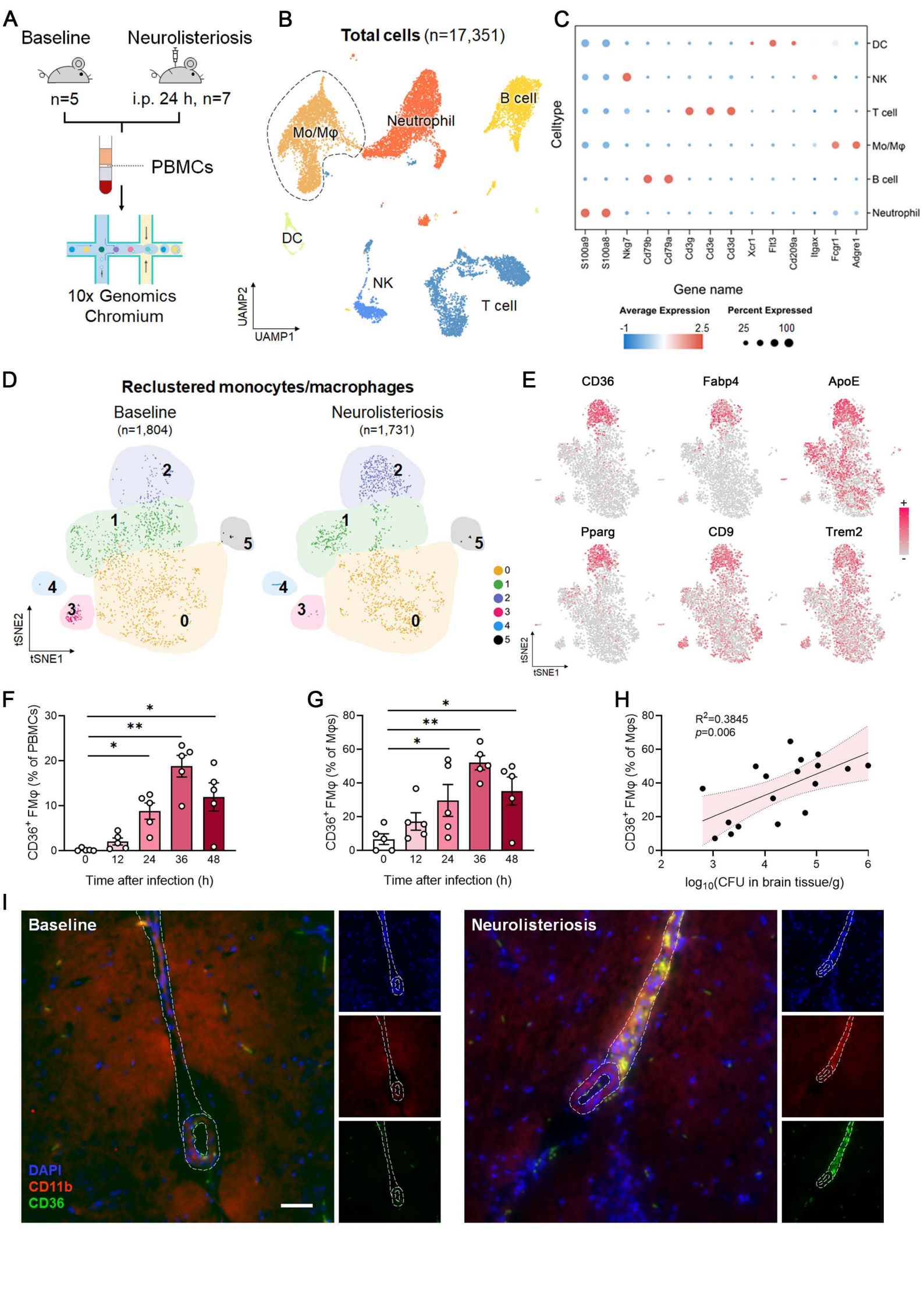
A
Baseline
Neurolisteriosis
n=5
i.p. 24 h, n=7
PBMCs
10x Genomics Chromium
B
Total cells (n=17,351)
Mo/Mφ
Neutrophil
B cell
DC
NK
T cell
UAMP2
UAMP1
C
Celltype
DC
NK
T cell
Mo/Mφ
B cell
Neutrophil
S100a9
S100a8
Nkg7
Cd79b
Cd79a
Cd3g
Cd3e
Cd3d
Xcr1
Flt3
Cd209a
Itgax
Fcgr1
Adgre1
Gene name
Average Expression
-1
2.5
Percent Expressed
25
100
D
Reclustered monocytes/macrophages
Baseline
(n=1,804)
Neurolisteriosis
(n=1,731)
tSNE2
tSNE1
E
CD36
Fabp4
ApoE
Pparg
CD9
Trem2
F
CD36+ FMφ (% of PBMCs)
Time after infection (h)
G
CD36+ FMφ (% of Mφs)
Time after infection (h)
H
R2=0.3845
p=0.006
CD36+ FMφ (% of Mφs)
log10(CFU in brain tissue/g)
I
Baseline
Neurolisteriosis
DAPI
CD11b
CD36

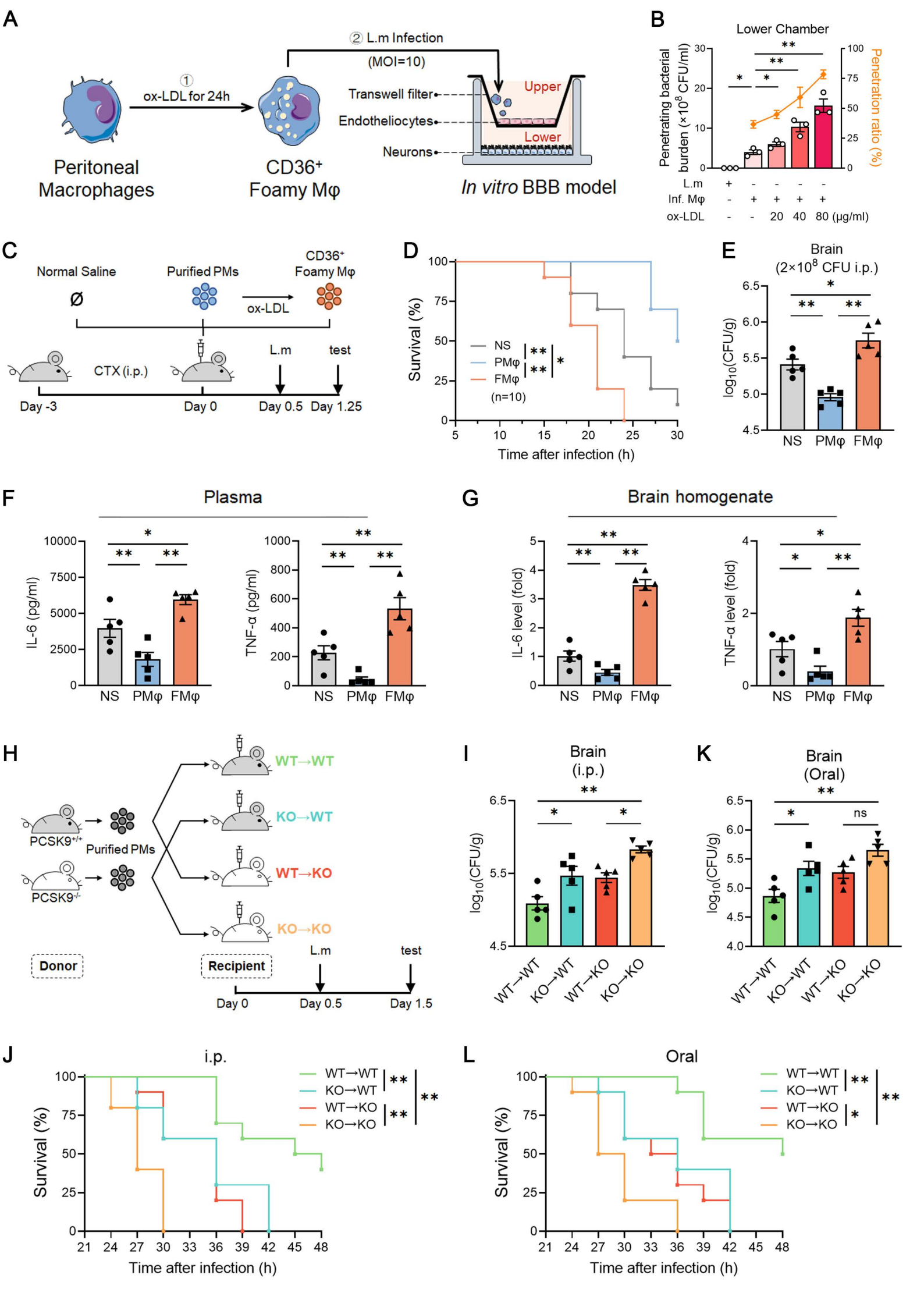
A
① ox-LDL for 24h
② L.m Infection (MOI=10)
Peritoneal Macrophages
CD36⁺ Foamy Mφ
Transwell filter
Endotheliocytes
Neurons
Upper
Lower
In vitro BBB model
B
Lower Chamber
Penetrating bacterial burden (×10⁸ CFU/ml)
Penetration ratio (%)
L.m
Inf. Mφ
ox-LDL
20 40 80 (μg/ml)
C
Normal Saline
Purified PMs
CD36⁺ Foamy Mφ
ox-LDL
CTX (i.p.)
L.m
test
Day -3
Day 0
Day 0.5
Day 1.25
D
Survival (%)
NS
PMφ
FMφ
(n=10)
Time after infection (h)
E
Brain (2×10⁸ CFU i.p.)
log10(CFU/g)
NS
PMφ
FMφ
F
Plasma
IL-6 (pg/ml)
TNF-α (pg/ml)
G
Brain homogenate
IL-6 level (fold)
TNF-α level (fold)
H
PCSK9⁺/⁺
PCSK9⁻/⁻
Purified PMs
WT→WT
KO→WT
WT→KO
KO→KO
Donor
Recipient
L.m
test
Day 0
Day 0.5
Day 1.5
I
Brain (i.p.)
K
Brain (Oral)
ns
J
i.p.
Survival (%)
Time after infection (h)
L
Oral

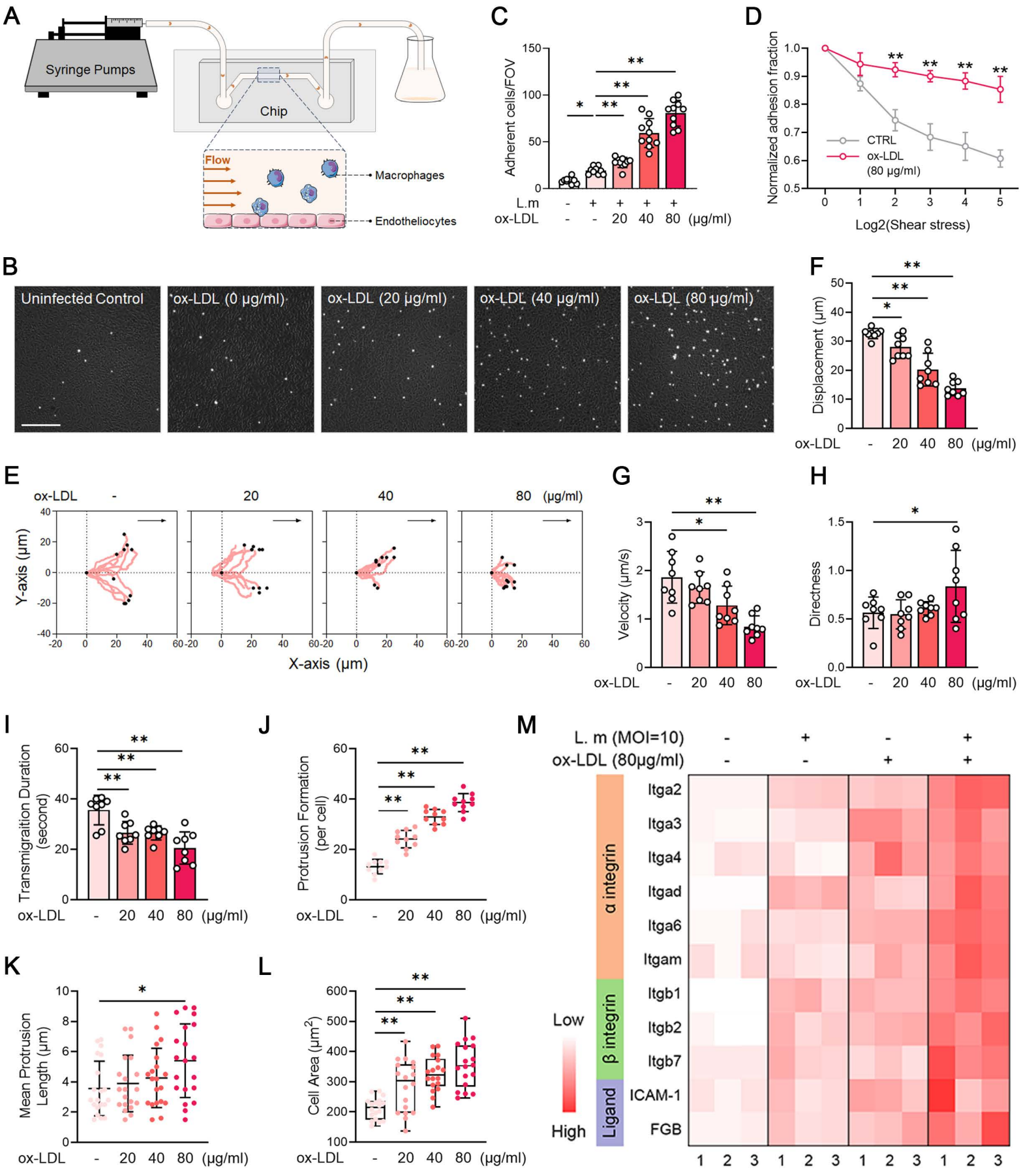
A
Syringe Pumps
Chip
Flow
Macrophages
Endotheliocytes
C
Adherent cells/FOV
L.m
ox-LDL
(μg/ml)
D
Normalized adhesion fraction
CTRL
ox-LDL
(80 μg/ml)
Log2(Shear stress)
B
Uninfected Control
ox-LDL (0 μg/ml)
ox-LDL (20 μg/ml)
ox-LDL (40 μg/ml)
ox-LDL (80 μg/ml)
F
Displacement (μm)
E
Y-axis (μm)
X-axis (μm)
G
Velocity (μm/s)
H
Directness
I
Transmigraition Duration (second)
J
Protrusion Formation (per cell)
K
Mean Protrusion Length (μm)
L
Cell Area (μm²)
M
L. m (MOI=10)
ox-LDL (80μg/ml)
α integrin
β integrin
Ligand
Itga2
Itga3
Itga4
Itgad
Itga6
Itgam
Itgb1
Itgb2
Itgb7
ICAM-1
FGB
Low
High

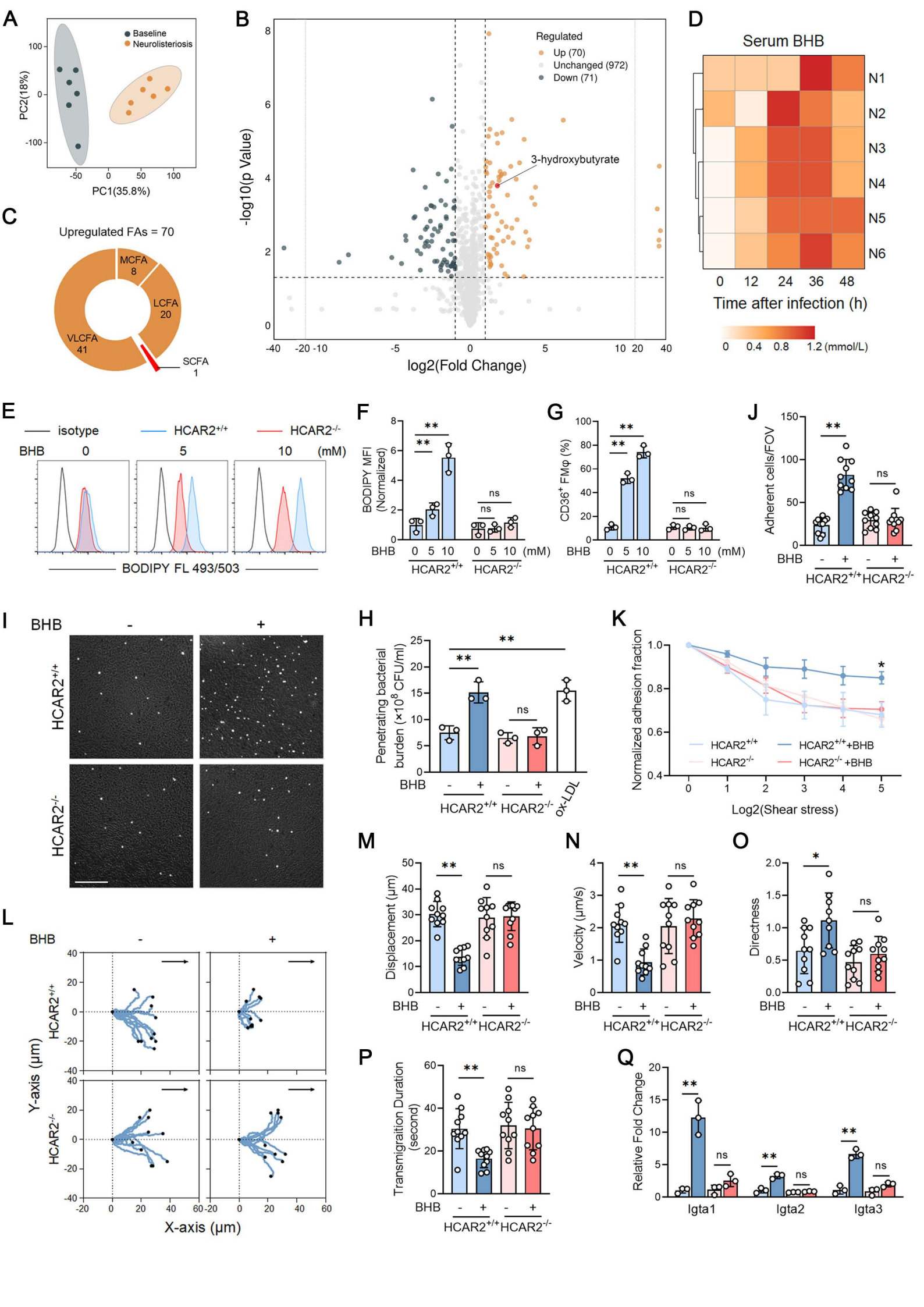
A
Baseline
Neurolisteriosis
PC2(18%)
PC1(35.8%)
B
Regulated
Up (70)
Unchanged (972)
Down (71)
3-hydroxybutyrate
-log10(p Value)
log2(Fold Change)
C
Upregulated FAs = 70
MCFA 8
LCFA 20
VLCFA 41
SCFA 1
D
Serum BHB
N1
N2
N3
N4
N5
N6
Time after infection (h)
(mmol/L)
E
isotype
HCAR2+/+
HCAR2-/-
BHB
(mM)
BODIPY FL 493/503
F
BODIPY MFI (Normalized)
G
CD36+ FMφ (%)
J
Adherent cells/FOV
I
BHB
HCAR2+/+
HCAR2-/-
H
Penetrating bacterial burden (×10^8 CFU/ml)
ox-LDL
K
Normalized adhesion fraction
Log2(Shear stress)
HCAR2+/++BHB
HCAR2-/- +BHB
L
Y-axis (μm)
X-axis (μm)
M
Displacement (μm)
N
Velocity (μm/s)
O
Directness
P
Transmigraition Duration (second)
Q
Relative Fold Change
Igta1
Igta2
Igta3

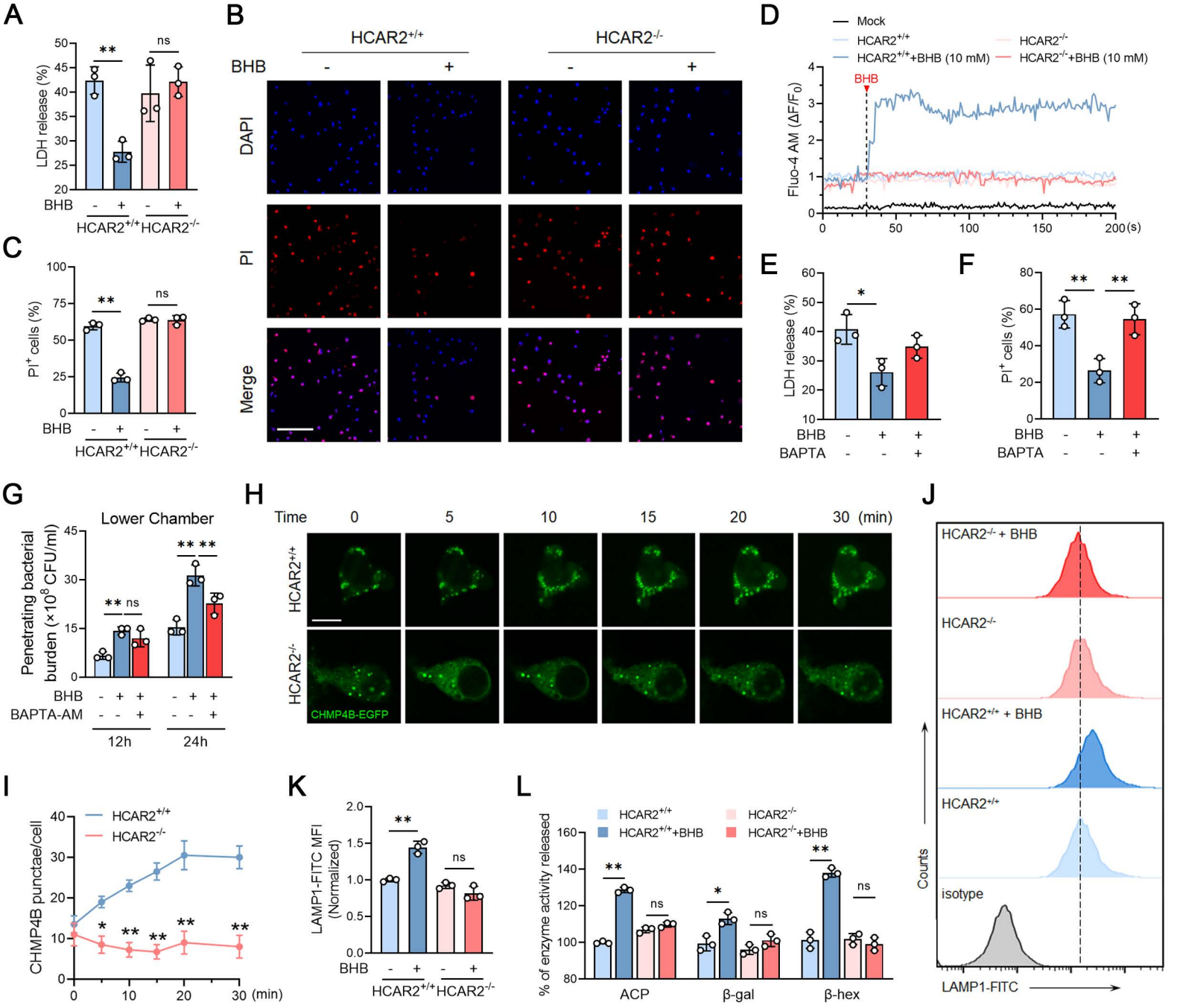
A
LDH release (%)
BHB
HCAR2+/+ HCAR2-/-
B
HCAR2+/+
HCAR2-/-
BHB
DAPI
PI
Merge
C
PI+ cells (%)
D
Mock
HCAR2+/+
HCAR2-/-
HCAR2+/+ +BHB (10 mM)
HCAR2-/- +BHB (10 mM)
BHB
Fluo-4 AM (ΔF/F0)
E
LDH release (%)
BAPTA
F
PI+ cells (%)
G
Lower Chamber
Penetrating bacterial burden (×10^8 CFU/ml)
BAPTA-AM
12h
24h
H
Time
0
5
10
15
20
30 (min)
CHMP4B-EGFP
I
CHMP4B punctae/cell
(min)
J
HCAR2-/- + BHB
HCAR2-/-
HCAR2+/+ + BHB
HCAR2+/+
isotype
Counts
LAMP1-FITC
K
LAMP1-FITC MFI (Normalized)
L
% of enzyme activity released
ACP
β-gal
β-hex

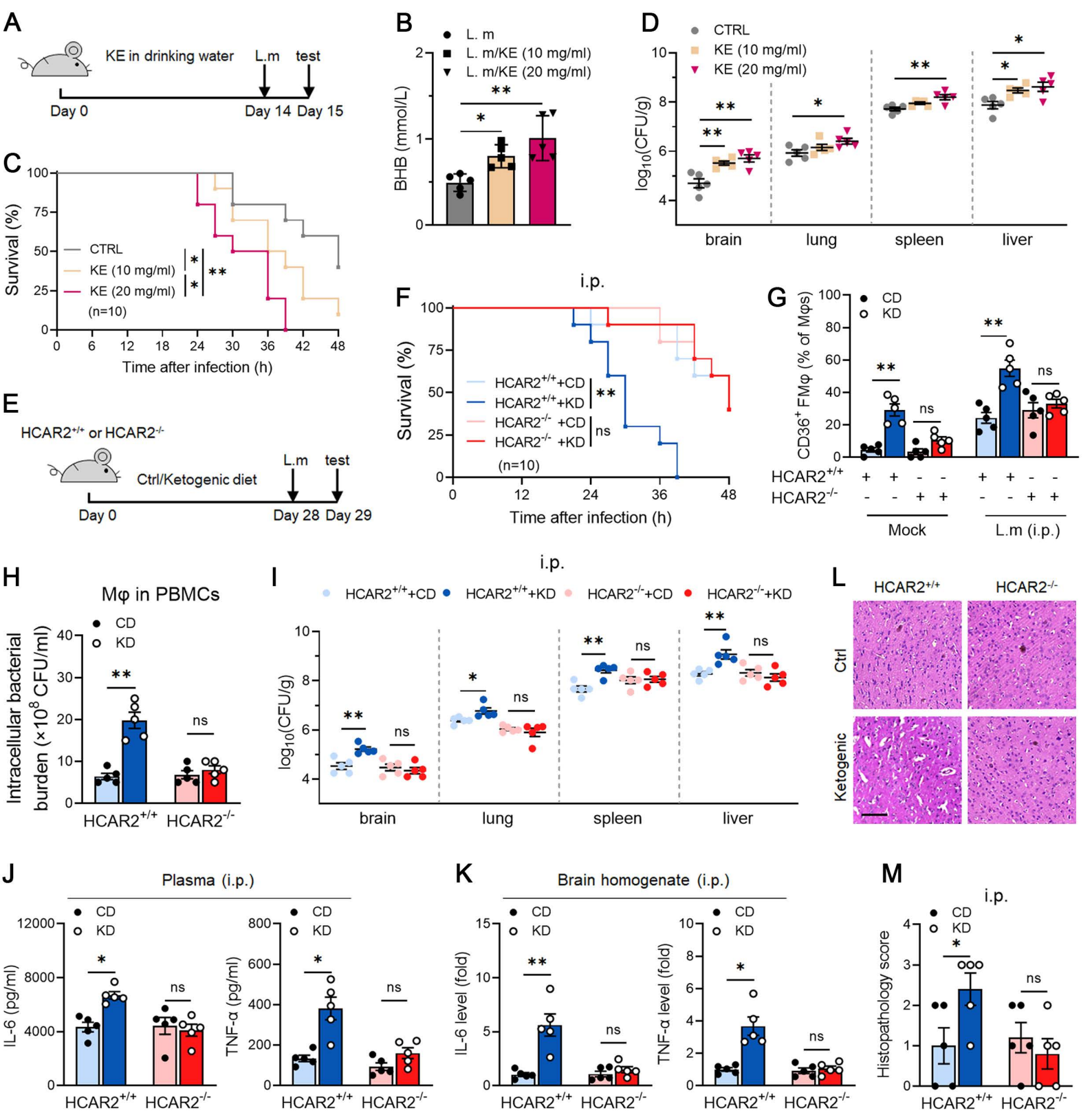
A
KE in drinking water
L.m
test
Day 0
Day 14
Day 15
B
L. m
L. m/KE (10 mg/ml)
L. m/KE (20 mg/ml)
BHB (mmol/L)
D
CTRL
KE (10 mg/ml)
KE (20 mg/ml)
log10(CFU/g)
brain
lung
spleen
liver
C
Survival (%)
CTRL
KE (10 mg/ml)
KE (20 mg/ml)
(n=10)
Time after infection (h)
E
HCAR2+/+ or HCAR2-/-
Ctrl/Ketogenic diet
L.m
test
Day 0
Day 28
Day 29
F
i.p.
Survival (%)
HCAR2+/+ +CD
HCAR2+/+ +KD
HCAR2-/- +CD
HCAR2-/- +KD
(n=10)
Time after infection (h)
G
CD
KD
CD36+ FMφ (% of Mφs)
HCAR2+/+
HCAR2-/-
Mock
L.m (i.p.)
H
Mφ in PBMCs
CD
KD
Intracellular bacterial burden (×10^8 CFU/ml)
HCAR2+/+
HCAR2-/-
I
i.p.
HCAR2+/+ +CD
HCAR2+/+ +KD
HCAR2-/- +CD
HCAR2-/- +KD
log10(CFU/g)
brain
lung
spleen
liver
L
HCAR2+/+
HCAR2-/-
Ctrl
Ketogenic
J
Plasma (i.p.)
CD
KD
IL-6 (pg/ml)
TNF-α (pg/ml)
HCAR2+/+
HCAR2-/-
K
Brain homogenate (i.p.)
CD
KD
IL-6 level (fold)
TNF-α level (fold)
HCAR2+/+
HCAR2-/-
M
i.p.
CD
KD
Histopathology score
HCAR2+/+
HCAR2-/-

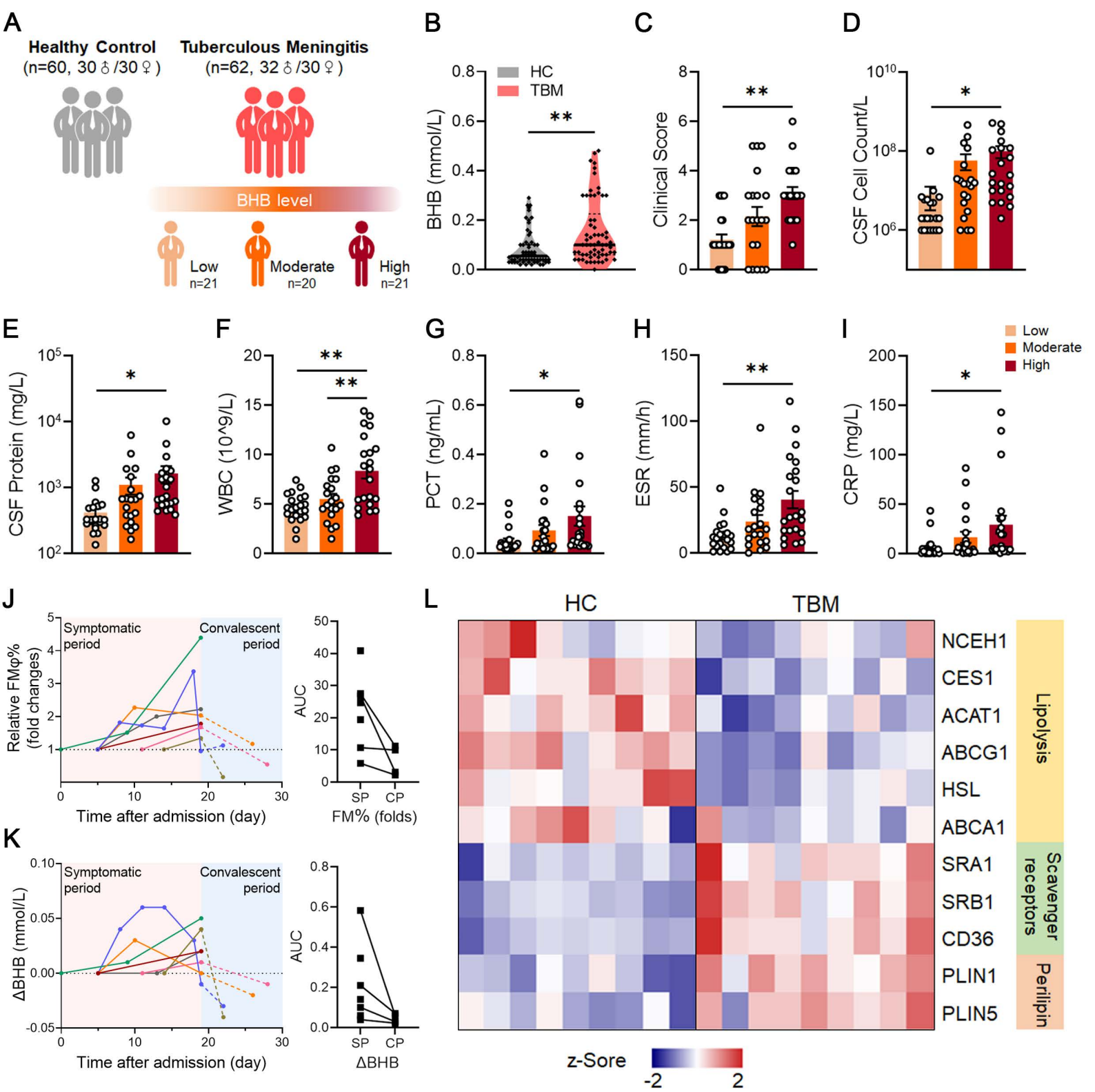
A
Healthy Control
(n=60, 30♂/30♀)
Tuberculous Meningitis
(n=62, 32♂/30♀)
BHB level
Low
n=21
Moderate
n=20
High
n=21
B
HC
TBM
BHB (mmol/L)
C
Clinical Score
D
CSF Cell Count/L
E
CSF Protein (mg/L)
F
WBC (10^9/L)
G
PCT (ng/mL)
H
ESR (mm/h)
I
CRP (mg/L)
Low
Moderate
High
J
Symptomatic period
Convalescent period
Relative FMφ% (fold changes)
Time after admission (day)
AUC
SP
CP
FM% (folds)
K
ΔBHB (mmol/L)
ΔBHB
L
HC
TBM
NCEH1
CES1
ACAT1
ABCG1
HSL
ABCA1
SRA1
SRB1
CD36
PLIN1
PLIN5
Lipolysis
Scavenger receptors
Perilipin
z-Sore
-2
2